

FINAL REPORT

Meshfree Modeling of Munitions Penetration in Soils

SERDP Project MR-2628

APRIL 2017

Dr. Sheng-Wei Chi
University of Illinois at Chicago

Distribution Statement A
This document has been cleared for public release



Page Intentionally Left Blank

This report was prepared under contract to the Department of Defense Strategic Environmental Research and Development Program (SERDP). The publication of this report does not indicate endorsement by the Department of Defense, nor should the contents be construed as reflecting the official policy or position of the Department of Defense. Reference herein to any specific commercial product, process, or service by trade name, trademark, manufacturer, or otherwise, does not necessarily constitute or imply its endorsement, recommendation, or favoring by the Department of Defense.

Page Intentionally Left Blank

REPORT DOCUMENTATION PAGE

*Form Approved
OMB No. 0704-0188*

Public reporting burden for this collection of information is estimated to average 1 hour per response, including the time for reviewing instructions, searching existing data sources, gathering and maintaining the data needed, and completing and reviewing this collection of information. Send comments regarding this burden estimate or any other aspect of this collection of information, including suggestions for reducing this burden to Department of Defense, Washington Headquarters Services, Directorate for Information Operations and Reports (0704-0188), 1215 Jefferson Davis Highway, Suite 1204, Arlington, VA 22202-4302. Respondents should be aware that notwithstanding any other provision of law, no person shall be subject to any penalty for failing to comply with a collection of information if it does not display a currently valid OMB control number. **PLEASE DO NOT RETURN YOUR FORM TO THE ABOVE ADDRESS.**

1. REPORT DATE (DD-MM-YYYY) 02-06-2017			2. REPORT TYPE Final Report		3. DATES COVERED (From - To)	
4. TITLE AND SUBTITLE Meshfree Modeling of Munitions Penetration in Soils			5a. CONTRACT NUMBER			
			5b. GRANT NUMBER			
			5c. PROGRAM ELEMENT NUMBER			
6. AUTHOR(S) Sheng-Wei Chi			5d. PROJECT NUMBER			
			5e. TASK NUMBER			
			5f. WORK UNIT NUMBER			
7. PERFORMING ORGANIZATION NAME(S) AND ADDRESS(ES) University of Illinois, Chicago 842 W Taylor Street, 3087 ERF Chicago, IL 60607			8. PERFORMING ORGANIZATION REPORT NUMBER			
9. SPONSORING / MONITORING AGENCY NAME(S) AND ADDRESS(ES) Strategic Environmental Research & Development Program 4800 Mark Center Drive, Suite 17D03 Alexandria, VA 22350			10. SPONSOR/MONITOR'S ACRONYM(S) SERDP			
			11. SPONSOR/MONITOR'S REPORT NUMBER(S) MR-2628			
12. DISTRIBUTION / AVAILABILITY STATEMENT Unlimited						
13. SUPPLEMENTARY NOTES						
14. ABSTRACT The objective of this proposal is to develop physically based models to predict the penetration depth of common military munitions in various soil conditions. Ultimately, the models will be used to determine probable depths of munitions in the soil of formerly used defense sites in support of planning for remediation. The simulation results can be used to aid sensor detection and removal of these munitions.						
15. SUBJECT TERMS						
16. SECURITY CLASSIFICATION OF:			17. LIMITATION OF ABSTRACT	18. NUMBER OF PAGES	19a. NAME OF RESPONSIBLE PERSON Sheng-Wei Chi	
a. REPORT u	b. ABSTRACT u	c. THIS PAGE u	u	75	19b. TELEPHONE NUMBER (include area code) 312-996-2426	

Page Intentionally Left Blank

Table of Contents

Table of Contents.....	i
List of Tables	iii
List of Figures	iv
List of Acronyms	vi
Keywords	vii
Acknowledgements.....	viii
1. Abstract.....	1
2. Objective	3
3. Background	4
4. Materials and Methods.....	7
4.1. Semi-Lagrangian RK framework for penetration modeling	7
4.1.1. Semi-Lagrangian RK Approximation	7
4.1.2. Single-field Semi-Lagrangian RK Formulation	8
4.1.3. Two-field ($u-p$) Semi-Lagrangian RK Formulation	10
4.1.4. Domain integration in the Galerkin formulation	12
4.2. Soil constitutive models	14
4.2.1. Non-associated Drucker-Prager with damage model	14
4.2.2. Three-invariant Soil Constitutive Model.....	15
5. Results and Discussion	23
5.1. Verifications	23
5.1.1. Uniaxial compression test.....	23
5.1.2. Triaxial compression test.....	27
5.1.3. Uniaxial extension test.....	31
5.1.4. Combined compression-shear test.....	32
5.1.5. Discussions	33
5.2. <i>Ad hoc</i> projectile penetration in soil simulations	34
5.3. Simulations of spherical ball drop test	51
5.3.1. Discussion.....	56
6. Conclusions and Implications for Future Research/Implementation.....	57
6.1. Conclusions:	57

6.2. Future Research/Implementation:	58
6.2.1. Infinite boundary in meshfree framework	58
6.2.2. Gradient enhanced stability and quasi linear formulation	58
6.2.3. Regularization for damaged/softened material behaviors	58
6.2.4. Constitutive Model Improvements	59
6.2.5. Numerical Implementation Improvements for soil models	59
6.2.6. Multiscale material modeling for calibration of material properties	60
6.2.7. Parametric studies and suggestion of penetration equations	60
7. Literature Cited	61
8. Appendices.....	66
A. Supporting Data:.....	66
B. List of Scientific/Technical Publications.....	66
Peer-reviewed journals:	66
Conference abstracts:.....	66
C. Other Supporting Materials	66

List of Tables

Table 1. Material properties for the Drucker-Prager uniaxial compression test.....	24
Table 2. Material properties for the three-invariant plasticity uniaxial compression test.	26
Table 3. Material properties for the Drucker-Prager triaxial compression test.	28
Table 4. Material properties for the three-invariant plasticity triaxial compression test.	30
Table 5. Problem setup of projectile penetration in soil	35
Table 6. Material properties of projectile	37
Table 7. Material properties of soil.....	37
Table 8. Projectile's maximum penetration depth for different impact angles.....	39
Table 9. Initial position & Velocity for spherical ball	53
Table 10. Drucker-Prager parameters & properties	53
Table 11. Spherical ball mechanical properties	53
Table 12. normalized total drop height and penetration depth	56

List of Figures

Figure 1. Semi-Lagrangian Reproducing Kernel (RK) and meshfree discretization.....	8
Figure 2. Nodal smoothing domain for the modified stabilized nonconforming nodal integration	14
Figure 3. Shear failure surface F_f	16
Figure 4. Evolution of C with respect to γ , (b) Evolution of Ξ with respect to γ	18
Figure 5. Uniaxial compression test. Dimensions, loading, and boundary conditions.....	23
Figure 6. Drucker-Prager and uniaxial compression test. Compressive axial stress vs. compressive axial strain response for FEM and mesh-free.	25
Figure 7. Three-invariant plasticity and uniaxial compression test. Compressive axial stress vs. compressive axial strain for FEM and mesh-free.	27
Figure 8. Triaxial compression test. Dimensions, loading, and boundary conditions.....	27
Figure 9. Drucker-Prager and triaxial compression test. (a) Strain rate vs. time, (b) Imposed displacement vs. step number.	28
Figure 10. Drucker-Prager and triaxial compression test. Compressive axial stress vs. compressive axial strain.	29
Figure 11. Three-invariant plasticity and triaxial compression test. Compressive axial stress vs. compressive axial strain.....	31
Figure 12. Uniaxial extension test. Dimensions, loading, and boundary conditions.....	31
Figure 13. Three-invariant plasticity and uniaxial extension test. Axial stress vs. axial strain for FEM and mesh-free.....	32
Figure 14. Combined compression-shear test. Dimensions, loading, and boundary conditions for (a) compression step, (b) shear step.	33
Figure 15. Three-invariant plasticity and combined compression-shear test. Shear stress vs. shear strain for FEM and mesh-free.	33
Figure 16. Dimension of projectile	36
Figure 17. Discretization for the projectile and the soil.....	36
Figure 18. Deformation of penetration in soil (impact angle 90°)	39
Figure 19. Trajectory and time history of penetration (impact angle 90°). (a) tip trajectory, (b) horizontal displacement history, (c) vertical displacement history, (d) horizontal velocity history, (c) vertical velocity history	40
Figure 20. Deformation of penetration in soil (impact angle 80°)	41
Figure 21. Trajectory and time history of penetration (impact angle 80°). (a) tip trajectory, (b) horizontal displacement history, (c) vertical displacement history, (d) horizontal velocity history, (c) vertical velocity history	42
Figure 22. Deformation of penetration in soil (impact angle 70°)	43
Figure 23. Trajectory and time history of penetration (impact angle 70°). (a) tip trajectory, (b) horizontal displacement history, (c) vertical displacement history, (d) horizontal velocity history, (c) vertical velocity history	44
Figure 24. Deformation of penetration in soil (impact angle 60°)	45
Figure 25. Trajectory and time history of penetration (impact angle 60°). (a) tip trajectory, (b) horizontal displacement history, (c) vertical displacement history, (d) horizontal velocity history, (c) vertical velocity history	46

Figure 26. Deformation of penetration in soil (impact angle 45°).....	47
Figure 27. Trajectory and time history of penetration (impact angle 45°). (a) tip trajectory, (b) horizontal displacement history, (c) vertical displacement history, (d) horizontal velocity history, (c) vertical velocity history	48
Figure 28. Deformation of penetration in soil (impact angle 30°).....	49
Figure 29. Trajectory and time history of penetration (impact angle 30°). (a) tip trajectory, (b) horizontal displacement history, (c) vertical displacement history, (d) horizontal velocity history, (c) vertical velocity history	50
Figure 30. Experimental setup (Seguin, et al 2008).....	52
Figure 31. (a) Spherical ball mesh configuration. (b) glass beads medium mesh configuration. (c) Initial ball's position in the numerical model.....	54
Figure 32. Case1; 500(mm) drop height	55
Figure 33. Case2; 300(mm) drop height	55
Figure 34. Case3; 100(mm) drop height	55
Figure 35. Penetration history for drop test	56

List of Acronyms

- DEM: discrete element methods
FEM: finite element methods
MSNNI: modified stabilized nonconforming nodal integration
RK: reproducing kernel
RKPM: reproducing kernel particle method
SCNI: stabilized conforming nodal integration
SNNI: stabilized nonconforming nodal integration
VCI: variationally consistent integration

Keywords

meshfree, u-p formulation, soil model, three invariant viscoplasticity, penetration, impact

Acknowledgements

The support from the Strategic Environmental Research and Development Program under the direction of Dr. Herb Nelson is acknowledged.

Meshfree Modeling of Munitions Penetration in Soils

Sheng-Wei Chi, Craig Foster, Ashkan Mahdavi, S. Milad Parvaneh, Thanakorn Siriaksorn

Department of Civil and Materials Engineering
University of Illinois at Chicago, Chicago, IL 60607
swchi@uic.edu

1. Abstract

Objective:

The objective of this proposal is to develop physically based models to predict the penetration depth of common military munitions in various soil conditions. Ultimately, the models will be used to determine probable depths of munitions in the soil of formerly used defense sites in support of planning for remediation. The simulation results can be used to aid sensor detection and removal of these munitions.

Technical Approach:

To model munitions penetration, a meshfree framework based on the Reproducing Kernel Particle Method (RKPM) is developed for handling extremely large deformation. A particle-to-particle based contact algorithm is introduced to efficiently capture energy and momentum exchanges between munitions and soils and between soil fragments. A two-field (displacement and pressure) semi-Lagrangian formulation is developed and implemented in consideration of porous nature of soils. Stabilized nodal domain integration schemes that ensure the accuracy and stability of the numerical solution is developed for the two-field Galerkin formulation.

To accurately represent the behavior of the soil, a viscoplasticity model is developed with regularized softening to account for large deformation of the soils. The model accounts for the behaviors seen in penetrations problems, including nonlinear pressure sensitivity of shear strength, rate dependence, shear-enhanced dilation, and a compaction hardening due to pore collapse and grain crushing. The model is updated with a regularized softening with increasing porosity that can naturally transition to more fluid-like flow, including liquefaction that is sometimes observed during penetration. The viscoplasticity model is embedded in a saturated two-field meshfree code, with partially saturated framework to be completed in subsequent research.

Results:

The two-field (displacement-pressure) formulation based on the Biot theory has been developed and implemented under the semi-Lagrangian RK framework, where displacement and pressure field are independently approximated by the semi-Lagrangian Reproducing Kernel (RK) shape functions. Some numerical schemes originally designed for the single-field formulation have been modified and implemented for the two-field formulation, including the modified stabilized non-conforming nodal

integration for the domain integration, stress update, and kernel contact algorithms. The central difference and forward Euler temporal integration schemes have been applied to the displacement and pressure fields, respectively, in the two-field formulation, leading to an explicit time marching scheme.

The three-invariant viscoplasticity model has been developed to effectively integrate tensile, shear, and compressive behavior. The evolution of volumetric plastic strain has been explicitly connected to the void ratio, allowing the model to be integrated with a poromechanical framework. Novel hardening/softening laws have been added to characterize strengthening and weakening in different loading regimes, and regularized the softening using viscoplasticity. The model also accounts for rate effects, differences in strength in triaxial extension and compression, compression hardening, and other effects. An efficient implementation using the spectral decomposition has been employed to reduce the cost of the complicated model.

The model has been verified against a Drucker-Prager model, and the meshfree and finite element implementations have been verified against each other to ensure proper implementation. The behaviors of the model have been demonstrated in a numerical framework using reasonably simple example problems. The developed two-field meshfree code have been employed to simulate penetration process into soil and predict the final penetration depth under different penetration angles. In the penetration simulations, the numerical results show that the maximum penetration depth varies from 3m to 1m with penetration angles ranging from 90° to 45° . The deformation of soil, e.g. soil splashing on the free surface, reflects the experiment observations after impact.

Benefits:

The project will benefit Department of Defense by providing a robust numerical framework for modeling penetration into soils. Eventually, the results of the simulations will translate into a set of tables for probable depths of munitions based on soil conditions, projectile type, and firing conditions.

The modeling will also have broader impacts to the engineering and scientific communities. The framework will be able to model other penetration scenarios for soil, rock, and concrete, for applications as diverse as deep penetrators designed to target underground bunkers to meteor impacts on extraterrestrial bodies. The constitutive models will further our fundamental understanding of soil behavior as we move toward physically based models for capturing observed soil responses. In addition, the numerical algorithms will enhance the set of tools available to solve many physical problems, especially those involved large deformation, material separation, and coupled physics problems.

2. Objective

The objective of this project is aimed to develop a meshfree method for soil-munitions interaction in order to predict penetration depth for a range of characteristics. The numerical framework for modeling the impact/penetration is based on the RKPM. This method has the advantages that it can model extreme distortion and material separation with relative ease and that it can directly incorporate the physically based soil constitutive models. Moreover, as a continuum approach, the computation cost in the current framework is more manageable in comparison to discrete element methods. These features are essential for creating an accurate, tractable, and physically based model of projectile penetration.

Equally important to developing a broadly applicable computing framework is modeling the material behavior. A constitutive model for the soil, a three-invariant viscoplasticity model, is adapted to reproduce the physical behaviors of soils, including hardening, softening, and rate dependency. This solid soil model is currently implemented in the displacement based formulation, and will be embedded in a poromechanical framework to reproduce the effects of water in the soil in the future.

Ultimately, the developed meshfree framework with the soil model is used to simulate penetration of munitions into soils for a range of soil and munitions parameters, velocities and impact angles. In the future, the outputs of these simulations will be used to create tables or regression curves of probable depths based on soil parameters that can be measured by standard laboratory tests, known munitions characteristics, and the scenarios under which those projectiles were launched.

The soil model is developed from the Sandia Geomodel (Fossum and Brannon 2004a and 2004b, Foster et al., 2005, Motamedi and Foster, 2017). This model accounts for many aspects of soil mechanical behavior, including rate dependence, difference in triaxial extension and compression strength, kinematic hardening and nonassociative dilation at low mean stresses, compaction hardening at high mean stress, and other features. The model will need to be extended to include poromechanical effects under saturated conditions (unsaturated behavior will be left for future work) directly related to material porosity. The model will also be extended to the finite deformation regime.

The completed model will be validated against both laboratory experiments (Seguin, et al. 2008) and field data (Christiensen, 1989) both for dry and saturated soils. The models will be adjusted until reasonable predictive agreement about penetration depths, within 20% relative error, can be obtained over a variety of conditions. These models will serve as a baseline for a future extension to partial saturation, and eventually the production of tables for determination of depth for a variety of conditions.

3. Background

The penetration of projectiles into the earth is a widely studied but complex problem. The impact of bodies into soil and rock has a wide variety of applications, from the study of meteor impacts to military applications to civilian engineering problems such as deep compaction. In military applications, there are a wide variety of scenarios, from deep penetrators designed for underground bunkers to impacts of accidental crashes.

In this objective of the SEED project is to examine the penetration of munitions at formerly used military test sites. The purpose of this examination is to determine the probable depth of buried projectiles so that they may be easily detected and removed as the site is remediated. The determination of the final depth is a complex task. It depends soil constituents: grains of different sizes, shapes, chemical cohesion, and mineral content, as well as the soil state, including porosity and degree of saturation. Some of these properties change locally during an impact event through compaction, shearing, and grain crushing. The depth also depends on the shape, mass, and mechanical properties of the projectiles. Finally, the impact angle, velocity and angular velocity greatly influence the ultimate depth. (Omidvar et al., 2014)

Even well characterized, the ultimate outcome of a penetration event can be difficult to predict. The physics are complicated, and no analytical method could hope to accurately predict the outcome. Numerical techniques may be employed, but extreme deformation and complex physics makes the problem extremely challenging.

Experimental studies of penetration can be divided two categories: laboratory and field experiments. While laboratory experiments are more controlled and more data can be readily measured, they are generally limited in scale, and can be difficult to extrapolate to field-scale simulations. Despite greater uncertainty in material state, velocity, and other parameters in field experiments (which have similar uncertainty to sites to be remediated), they remain vital to validation. Laboratory experiments of penetration are subject to confining boundary conditions that can greatly affect penetration depth and the type of deformation of the soil particles (Seguin, et al 2008, Omidvar, et al 2014). The interactions are complex; however, and sometimes give difficult to interpret results (Borg, et al 2013). Ideally, fully transmitting boundary conditions would allow stress waves to propagate away from the projectile without reflection. Such boundary conditions are difficult to set up experimentally, however. Fortunately, numerical models can account for varying boundary conditions, and a physically based model can be validated in a controlled setting before being applied to more open field experiments. An excellent compilation of field data is the SAND Report, *Twenty five years of penetration records at Sandia National Laboratories-PENTDB: a relational database*, (Christiansen, 1989) though this document is limited release.

While, experiments are vital to understanding the behavior of penetration in soils, it is impossible to run experiments for every scenario at a test. Modeling is a cost-effective solution to capturing the response of projectile impact in soils. With regards to penetration depth, a number of phenomenological and semi-empirical methods have been developed, e.g. (Euler, 1914; Carter et al., 1986; Forrestal and Luk, 1992, Durbin and Masri, 2004; Salgado, et al., 1997; Yu and Houlsby, 1991). Many of these models are reviewed in Omidvar, et al., 2014. These models vary in the extent of the physics involved as well as the extent of validation, but it is impossible to solve all of the equations physically in a very general way that can be easily

extended to a variety of situations. Still, the models can provide good initial verification to numerical codes.

The equations for physics-based modeling of penetration are far too complex to be solved by analytical methods. Some simulations have been performed with finite element analysis. While the finite element method (FEM) has been used for a wide variety of mechanical and structural problems with great success, the penetration problem is not as easily solved. Due to challenges with material separation a narrow initial cavity is often assumed. Other challenges include very large distortion of the elements, which can lead to inaccurate results, and the evolving contact problem. Though a number of algorithms have been developed for contact, practical impact problems remain a challenge.

Recently, particle-based models, notably discrete or distinct element methods (DEM), have been used to examine soil deformation in the case of projectiles. Here the particles are modeled individually, usually with simple constitutive laws governing the stiffness between the individual particles. While computationally expensive, they have been used to model penetration in sands and gravels, e.g. (Tiwari et al., 2015; Borvik et al., 2015). Some approximate scaling laws are required for fine-grained soils, though it remains unclear how generally these apply to a range of loading scenarios. While the approach can capture some mesoscale phenomena such as the formation and buckling of force chains, challenges such as physically based grain fracture and sophisticated frictional interaction and wear of real grains remain. DEM have often been coupled with rigid or finite element models of the penetrators, e.g. Oñate and Rojek, 2004.

As opposed to DEM, meshfree methods based on the continuum theory, such as the Element-Free Galerkin method (Belytschko et al., 1994) and the RKPM (Liu et al., 1995) have gained popularity in modeling large deformation problems. Chen et al. (1996) introduced a consistent discrete formulation for RK approximation and extended the RK formulation to finite deformation problems. Guan et al. (2014) introduced the semi-Lagrangian RKPM formulation with the kernel contact algorithm under the meshfree framework. Bessa et al. (2014) established a direct link between the RKPM and the state-based peridynamics methods (Silling, 2000; Silling & Lehoucq, 2008) and concluded that the state-based peridynamics leads to an approximation of the derivatives that can be obtained from the RKPM. In the Galerkin numerical procedure, meshfree methods require high-order numerical integration on a background grid, resulting in considerable computation efforts (Dolbow and Belytschko, 1999). On the other hand, low-order numerical integration, such as nodal integration, leads to instability. In order to circumvent the numerical instability, Bonet et al. (1999) introduced a correction term into the derivative of shape function at nodal point by enforcing the linear exactness condition. Chen et al. (2001) proposed the Stabilized Conforming Nodal Integration (SCNI) in which the linear exactness is achieved in the Galerkin approximation of second order PDEs, and later applied SCNI to large deformation problems in Chen et al. (2002). Recently, Chen et al. (2013) generalized the SCNI and the idea of integration constraint and developed a variationally consistent integration scheme to achieve arbitrary order of exactness in the Galerkin formulation. A non-confirming counterpart of the SCNI, where the smoothed strain is constructed over non-confirming subdomains, has been introduced in concrete penetration modeling (Guan et al., 2011; Chi et al., 2015). Hillman et al. (2014) introduced stabilized integration schemes under the variationally consistent integration (VCI) framework for modeling impact and penetration problems. An implicit gradient stabilization was later introduced for enhanced stability in the Galerkin meshfree method when

the nodal integration is used (Hillman and Chen, 2016). Yreux and Chen (2017) introduced a new formulation to construct the Moving Least Squares|RK approximation even when the neighboring nodes are insufficient due to material separation.

The history of modern soil mechanics is relatively young, reaching back only a hundred years or so to Terzaghi's effective stress principle and one-dimensional consolidation theory. In the latter half of the twentieth century and into the twenty-first, however, and profusion of models have been introduced to capture various behaviors of soils.

Among continuum models, plasticity models and their extensions have been applied to a variety of applications with success. One of the first models was the Mohr-Coulomb model, developed from a failure condition for soils, and captures the mean stress-dependent shear strength of soil. Others, such as the Drucker-Prager and Lade-Duncan models, built on these characteristics while improving computational efficiency. The Drucker-Prager criterion (Drucker and Prager 1952), among others, is a suitable candidate as a preliminary constitutive model for many engineering applications due to its simplicity, smooth yield surface, relatively easy implementation and high efficiency within numerical algorithms. However, it has a few limitations, including overestimating strength in triaxial extension (Alejano, 2012) and being unable to model soil compaction at high mean stresses.

The original and modified Cam-Clay models (Roscoe and Burland, 1968), do account for both dilation and compaction and different mean stresses, but have limitations in the shape of the yield surface and are designed for slow consolidation behavior. A family of cap models has been developed for more general response of both soils and rock, some of which are discussed in (Fossum and Brannon 2004a). An enormous number of models have been developed to simulate various soil behaviors. An early review of soil plasticity models may be found in (Scott 1985), among other places. Important characteristics of accurate models include pressure dependence, which is nonlinear over large ranges, differences in triaxial extension and compression strength, and, at large pressures, the ability to capture inelastic compaction due to pore collapse and grain fracture. Rate dependent effects become important for applications involving high strain rates, including penetration.

4. Materials and Methods

4.1. Semi-Lagrangian RK framework for penetration modeling

4.1.1. Semi-Lagrangian RK Approximation

Penetration simulations involve extremely large deformation and highly fragmented configurations that are very difficult to capture with conventional finite element methods. Therefore, a meshfree framework based on the semi-Lagrangian RKPM (Guan et al., 2011; Chi et al., 2015, Chen et al., 2017) is introduced to effectively model excessive soil deformation.

Consider a set of NP scattered points in a closed domain, $\bar{\Omega}_x = \Omega_x \cup \partial\Omega_x$, with spatial positions in the initial configuration $\{\mathbf{X}_I\}_{I=1}^{NP}$, where $\partial\Omega_x$ is the boundary of the open domain Ω_x in the initial configuration. In this report, \mathbf{X} and X are designated for coordinates in the initial configuration whereas \mathbf{x} and x for coordinates in the current/deformed configuration. The two coordinates are related through a mapping $\mathbf{x} = \varphi(\mathbf{X}, t)$, and the material point in the current configuration is defined as $\mathbf{x}_I \equiv \varphi(\mathbf{X}_I, t)$. The semi-Lagrangian RK shape function is constructed following a material point \mathbf{x}_I while its domain of influence has fixed size and shape (Figure 1). The semi-Lagrangian RK approximation of a function $u(\mathbf{x})$ is expressed as:

$$u(\mathbf{x}) \approx \sum_{I=1}^{NP} \Psi_I(\mathbf{x}) d_I = \sum_{I=1}^{NP} C(\mathbf{x}; \mathbf{x} - \mathbf{x}_I) \phi_a(\mathbf{x} - \mathbf{x}_I) d_I. \quad (1)$$

where Ψ_I is the semi-Lagrangian shape function associated with node I and d_I is the corresponding coefficient. Above the kernel function $\phi_a(\mathbf{x} - \mathbf{x}_I)$ controls the smoothness and the domain of influence of the shape function with a support size a . The center of the kernel function follows the material point while its domain of influence is fixed in space. The correction function $C(\mathbf{x}; \mathbf{x} - \mathbf{x}_I)$ is introduced to ensure solution accuracy up to the desired order, and it is usually expressed by the linear combination of a set of m -th order complete monomials, that is

$$C(\mathbf{x}; \mathbf{x} - \mathbf{x}_I) = \sum_{|\beta|=0}^m (\mathbf{x} - \mathbf{x}_I)^\beta b_\beta(\mathbf{x}) \equiv \mathbf{H}(\mathbf{x} - \mathbf{x}_I) \mathbf{b}(\mathbf{x}) \quad (2)$$

where β is the multi-dimensional index, considering up to three dimensions: $\beta = (\beta_1, \beta_2, \beta_3)$ with its length defined as $|\beta| \equiv \sum_{i=1}^3 \beta_i$, $b_\beta \equiv b_{\beta_1 \beta_2 \beta_3}$ is the corresponding coefficient $(\mathbf{x} - \mathbf{x}_I)^\beta \equiv (x_1 - x_{1I})^{\beta_1} (x_2 - x_{2I})^{\beta_2} (x_3 - x_{3I})^{\beta_3}$, and $\mathbf{b}(\mathbf{x})$ and $\mathbf{H}(\mathbf{x} - \mathbf{x}_I)$ are the vector forms of b_β and $(\mathbf{x} - \mathbf{x}_I)^\beta$.

The coefficient $\mathbf{b}(\mathbf{x})$ can be determined by the reproducing condition:

$$\sum_{I=1}^{NP} \Psi_I(\mathbf{x}) \mathbf{x}_I^\beta = \mathbf{x}^\beta \quad ; \quad |\beta| \leq m, \quad (3)$$

and subsequently the RK shape function is given as follows.

$$\Psi_I(\mathbf{x}) = \mathbf{H}^T(\mathbf{0}) \mathbf{M}^{-1}(\mathbf{x}) \mathbf{H}(\mathbf{x} - \mathbf{x}_I) \phi_a(\mathbf{x} - \mathbf{x}_I) \quad (4)$$

where

$$\mathbf{M}(\mathbf{x}) = \sum_{I=1}^{NP} \mathbf{H}(\mathbf{x} - \mathbf{x}_I) \mathbf{H}^T(\mathbf{x} - \mathbf{x}_I) \phi_a(\mathbf{x} - \mathbf{x}_I) \quad (5)$$

It is noted that the kernel function abovementioned follows the material points while its domain of influence is fixed, which has been called the Eulerian kernel in literature. The influence of the Eulerian kernel can serve for contact detection in the points-based simulations (Li et al., 2001; Guan et al., 2011, Chi et al., 2015), and the semi-Lagrangian RK shape function inherits such property. Thus, several contacts algorithms have been introduced to impose contact conditions without a pre-defined contact surfaces under the semi-Lagrangian RK framework (Chi et al., 2015; Guan et al., 2011). Specially, a levelset-enhanced frictional kernel contact algorithm is adopted in this project. The details are referred to (Chi et al., 2015).

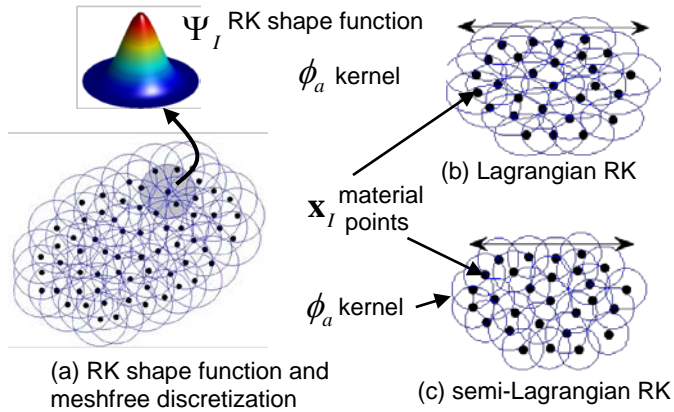


Figure 1. Semi-Lagrangian Reproducing Kernel (RK) and meshfree discretization

4.1.2. Single-field Semi-Lagrangian RK Formulation

The equation of motion of a deformable body in the current/deformed configuration with traction and displacement boundary conditions is given:

$$\begin{aligned} \rho \ddot{\mathbf{u}} &= \nabla \cdot \boldsymbol{\sigma} + \mathbf{b} && \text{in } \Omega_x \\ \mathbf{n} \cdot \boldsymbol{\sigma} &= \mathbf{h} && \text{on } \partial\Omega_x^h \\ \mathbf{u} &= \mathbf{g} && \text{on } \partial\Omega_x^g \end{aligned} \quad (6)$$

where ρ is the density; \mathbf{b} is the body force; \mathbf{u} is the displacement vector; $\boldsymbol{\sigma}$ is the Cauchy stress; Ω_x is the open domain in the current configuration with its enclosed boundary $\partial\Omega_x$; $\partial\Omega_x^h$ and $\partial\Omega_x^g$ are the boundaries with the prescribed traction \mathbf{h} and the prescribed displacement \mathbf{g} ,

respectively; and $\partial\Omega_x^h \cup \partial\Omega_x^g = \partial\Omega_x$, $\partial\Omega_x^h \cap \partial\Omega_x^g = \emptyset$. The variational equation of equation (6) is:

$$\int_{\Omega_x} \rho \delta \mathbf{u} \cdot \ddot{\mathbf{u}} d\Omega + \int_{\Omega_x} \delta \nabla \mathbf{u} \cdot \boldsymbol{\sigma} d\Omega = \int_{\Omega_x} \delta \mathbf{u} \cdot \mathbf{b} d\Omega + \int_{\partial\Omega_x^h} \delta \mathbf{u} \cdot \mathbf{h} d\Gamma. \quad (7)$$

The displacement \mathbf{u} and its variation $\delta \mathbf{u}$ are approximated using the semi-Lagrangian RK as in equation (1), and the associated velocity and acceleration are approximated by the material time derivatives of equation (1), leading to:

$$\dot{\mathbf{u}}^h(\mathbf{x}, t) = \mathbf{v}^h(\mathbf{x}, t) = \sum_{I=1}^{NP} (\Psi_I(\mathbf{x}) \dot{\mathbf{d}}(t) + \bar{\Psi}_I(\mathbf{x}) \mathbf{d}(t)), \quad (8)$$

$$\ddot{\mathbf{u}}^h(\mathbf{x}, t) = \mathbf{a}^h(\mathbf{x}, t) = \sum_{I=1}^{NP} (\Psi_I(\mathbf{x}) \ddot{\mathbf{d}}(t) + 2\bar{\Psi}_I(\mathbf{x}) \dot{\mathbf{d}}(t) + \bar{\bar{\Psi}}_I(\mathbf{x}) \mathbf{d}(t)). \quad (9)$$

Above the superscript h denotes the finite dimensional approximation; $\mathbf{d}(t)$, $\dot{\mathbf{d}}(t)$, and $\ddot{\mathbf{d}}(t)$ are the nodal coefficients of displacement, velocity, and acceleration, respectively; $\bar{\Psi}$ and $\bar{\bar{\Psi}}$ are the time rate changes due to the Eulerian kernel function, i.e.,

$$\dot{\phi}_a(\mathbf{x} - \mathbf{x}_I) = \dot{\phi}_a\left(\frac{\|\mathbf{x} - \mathbf{x}_I\|}{a}\right) = \phi'_a \frac{(\mathbf{x} - \mathbf{x}_I) \cdot (\mathbf{v} - \mathbf{v}_I)}{a \|\mathbf{x} - \mathbf{x}_I\|}. \quad (10)$$

Substituting equations (8) and (9) into the Galerkin form of equation (7), it leads to the semi-discrete equation in the matrix form as follows.

$$\mathbf{M} \ddot{\mathbf{d}}(t) + \mathbf{G} \dot{\mathbf{d}}(t) + \bar{\mathbf{G}} \mathbf{d}(t) = \mathbf{F}^{\text{ext}} - \mathbf{F}^{\text{int}}, \quad (11)$$

where

$$\mathbf{M}_{IJ} = \int_{\Omega_x} \rho \Psi_I \Psi_J \mathbf{I} d\Omega, \quad (12)$$

$$\mathbf{G}_{IJ} = \int_{\Omega_x} 2\rho \Psi_I \bar{\Psi}_J \mathbf{I} d\Omega, \quad (13)$$

$$\bar{\mathbf{G}}_{IJ} = \int_{\Omega_x} \rho \Psi_I \bar{\bar{\Psi}}_J \mathbf{I} d\Omega, \quad (14)$$

$$\mathbf{F}_I^{\text{ext}} = \int_{\Omega_x} \Psi_I \mathbf{b} d\Omega + \int_{\partial\Omega_x^h} \Psi_I \mathbf{h} d\Gamma, \quad (15)$$

$$\mathbf{F}_I^{\text{int}} = \int_{\Omega_x} \mathbf{B}_I^T \boldsymbol{\Sigma} d\Omega. \quad (16)$$

Above \mathbf{I} denotes the identity matrix, \mathbf{B}_I is the gradient matrix representing the symmetric part of $\nabla \mathbf{u}$ associated with node I , $\boldsymbol{\Sigma}$ is the stress vector associated with $\boldsymbol{\sigma}$. The matrices associated with the time rate change of the semi-Lagrangian kernels, \mathbf{G} , $\bar{\mathbf{G}}$, are usually omitted for computational efficiency since they have very subtle effects on the solutions when the nodal integration is used (Chi et al., 2015). Numerical time integration schemes, such as the Newmark methods, can then be introduced in equation (11) (see Siriaksorn et al., 2017 for details). In this

project the central difference is used for temporal integration for the displacement unless otherwise noted.

4.1.3. Two-field ($u-p$) Semi-Lagrangian RK Formulation

To account for the coupling effect between solid and fluid, a two-field meshfree formulation based on the Biot mixture theory (Biot, 1956) is developed and implemented. At the current stage, only fully saturated soil material is considered. The governing equations are the balance of momentum and continuity equation for the fluid phase, respectively:

$$\rho \ddot{\mathbf{u}} = \nabla \cdot \boldsymbol{\sigma} + \mathbf{b} , \quad \text{in } \Omega_x \quad (17)$$

$$\alpha \nabla \cdot \dot{\mathbf{u}} + \frac{\dot{P}}{M} + \nabla \cdot \mathbf{q} = 0 , \quad \text{in } \Omega_x \quad (18)$$

with boundary conditions:

$$\begin{aligned} \mathbf{n} \cdot \boldsymbol{\sigma} &= \mathbf{h} && \text{on } \partial\Omega_x^h \\ \mathbf{u} &= \mathbf{g} && \text{on } \partial\Omega_x^g \\ -\mathbf{n} \cdot \mathbf{q} &= v_s && \text{on } \partial\Omega_x^s \\ P &= \bar{P} && \text{on } \partial\Omega_x^r \end{aligned} \quad (19)$$

where ρ is the saturated density of the porous medium, α is the Biot coefficient, P is the pore pressure, M is the Biot compressibility modulus, and \mathbf{q} is the superficial velocity, v_s is the prescribed fluid inflow on $\partial\Omega_x^s$, \bar{P} is the prescribed pore fluid pressure on $\partial\Omega_x^r$, and

$\partial\Omega_x^s \cup \partial\Omega_x^r = \partial\Omega_x$, $\partial\Omega_x^s \cap \partial\Omega_x^r = \emptyset$. The total stress can be decomposed into partial stresses from solid and fluid, i.e., $\boldsymbol{\sigma} = (1-\lambda)\boldsymbol{\sigma}^s + \lambda\boldsymbol{\sigma}^F \mathbf{I}$, where $\boldsymbol{\sigma}^s$ is the solid stress, $\boldsymbol{\sigma}^F$ is the fluid stress, λ is the porosity, defined as the ratio of the void volume to the total volume V . Introducing the Biot coefficient α , the total stress can be alternatively represented as

$$\boldsymbol{\sigma} = \bar{\boldsymbol{\sigma}} - \alpha P \mathbf{I}, \quad (20)$$

where $\bar{\boldsymbol{\sigma}}$ is the effective stress of the solid phase. The soil constitutive law described in the following section will be introduced for determining the effective stress $\bar{\boldsymbol{\sigma}}$. The Biot coefficient α and Biot compressibility modulus M can be defined respectively as

$$\alpha = 1 - \frac{K}{K_s} , \quad (21)$$

$$\frac{1}{M} = \frac{\alpha - \lambda}{K_s} + \frac{\lambda}{K_f} , \quad (22)$$

where K is the bulk modulus of the porous medium; K_s is the bulk modulus of the solid grains; K_f is the bulk modulus of the fluid. For isotropic porous media, the relationship between the flux or superficial velocity \mathbf{q} and the pore pressure P can be described by using Darcy's law as

$$\mathbf{q} = -\frac{k}{\mu} (\nabla P - \rho_f \mathbf{g}), \quad (23)$$

where k is the intrinsic permeability, μ is the fluid dynamic viscosity, ρ_f is the fluid density, and \mathbf{g} is the gravity.

The variational form, and subsequently the Galerkin formulation, of (17) and (18) are given as follows.

$$\int_{\Omega_x} \delta \nabla \mathbf{u}^h : \bar{\boldsymbol{\sigma}}^h d\Omega - \int_{\Omega_x} \delta \nabla \cdot \mathbf{u}^h \alpha P^h d\Omega + \int_{\Omega_x} \delta \mathbf{u}^h \cdot \rho \ddot{\mathbf{u}}^h d\Omega = \int_{\partial \Omega_x^h} \delta \mathbf{u}^h \cdot \mathbf{h} d\Gamma + \int_{\Omega_x} \delta \mathbf{u}^h \cdot \mathbf{b} d\Omega, \quad (24)$$

$$\begin{aligned} & \int_{\Omega_x} \delta P^h \alpha \nabla \cdot \dot{\mathbf{u}}^h d\Omega - \int_{\Omega_x} \delta P^h \frac{\dot{P}^h}{M} d\Omega + \int_{\Omega_x} \frac{k}{\mu} \delta \nabla P^h \cdot \nabla P^h d\Omega \\ &= \int_{\partial \Omega_x^s} \delta P^h v_s d\Gamma + \int_{\Omega_x} \frac{k}{\mu} \rho_f \delta \nabla P^h \cdot \mathbf{g} d\Omega \end{aligned} . \quad (25)$$

The central difference and the forward Euler temporal integration schemes are employed for the displacement field and the pressure field, respectively, as follows.

$$\mathbf{d}_I^{n+1} = \mathbf{d}_I^n + \Delta t \mathbf{v}_I^n + 0.5 \Delta t^2 \mathbf{a}_I^n, \quad (26)$$

$$\mathbf{v}_I^{n+1} = \hat{\mathbf{v}}_I^{n+1} + 0.5 \Delta t \mathbf{a}_I^{n+1}, \quad (27)$$

$$p_I^{n+1} = p_I^n + \Delta t \dot{p}_I^n, \quad (28)$$

where Δt is the time step, the superscript n denotes the time step count, \mathbf{d} , \mathbf{v} , \mathbf{a} , and p are the nodal coefficients for displacement, velocity, acceleration, and fluid pressure, respectively. The predicted velocity $\hat{\mathbf{v}}_I^{n+1}$ is defined as

$$\hat{\mathbf{v}}_I^{n+1} = \mathbf{v}_I^n + 0.5 \Delta t \mathbf{a}_I^n \quad (29)$$

After introducing the semi-Lagrangian RK shape function (equation (1)) for the approximation functions of displacements \mathbf{u}^h and fluid pressure P^h and their time derivatives using equations (8) and (9), the equations (24) and (25) are recast into the matrix forms:

$$\mathbf{M} \mathbf{a}^{n+1} + \mathbf{G} \mathbf{v}^{n+1} + \bar{\mathbf{G}} \mathbf{d}^{n+1} = \mathbf{F}^{\text{ext}} - \bar{\mathbf{F}}^{\text{int}}, \quad (30)$$

$$\mathbf{S} \dot{\mathbf{p}}^{n+1} + \mathbf{Q} \mathbf{p}^{n+1} + \bar{\mathbf{Q}} \mathbf{d}^{n+1} = \tilde{\mathbf{F}}^{\text{ext}} - \tilde{\mathbf{F}}^{\text{int}}, \quad (31)$$

where \mathbf{M} , \mathbf{G} , $\bar{\mathbf{G}}$, and \mathbf{F}^{ext} are the same as in equations (12)-(15), and

$$S_{IJ} = \int_{\Omega_x} M^{-1} \Psi_I \Psi_J d\Omega, \quad (32)$$

$$Q_{IJ} = \int_{\Omega_x} M^{-1} \Psi_I \bar{\Psi}_J d\Omega, \quad (33)$$

$$\bar{\mathbf{Q}}_{IJ} = \int_{\Omega_x} \alpha \Psi_I \nabla \bar{\Psi}_J d\Omega, \quad (34)$$

$$\bar{\mathbf{F}}_I^{\text{int}} = \int_{\Omega_x} \nabla \Psi_I \cdot \bar{\boldsymbol{\sigma}}^{n+1} d\Omega - \int_{\Omega_x} \alpha \nabla \Psi_I P^{n+1} d\Omega - \int_{\Omega_x} \Psi_I \mathbf{b} d\Omega, \quad (35)$$

$$\tilde{F}_I^{\text{ext}} = \int_{\partial\Omega_x} \Psi_I v_s d\Gamma, \quad (36)$$

$$\tilde{F}_I^{\text{int}} = \int_{\Omega_x} \alpha \Psi_I \nabla \cdot \dot{\mathbf{u}}^{n+1} d\Omega + \int_{\Omega_x} (k/\mu) \nabla \Psi_I \cdot \nabla P^{n+1} d\Omega - \int_{\Omega} (k/\mu) \rho^f \nabla \Psi_I \cdot \mathbf{g} d\Omega. \quad (37)$$

Applying the central difference and forward Euler schemes in equations (26)-(29) leads to the full discrete equations:

$$(\mathbf{M} + 0.5\Delta t(\mathbf{C} + \mathbf{G}))\mathbf{a}^{n+1} = \mathbf{F}^{\text{ext}} - \bar{\mathbf{F}}^{\text{int}} - (\mathbf{C} + \mathbf{G})\hat{\mathbf{v}}^{n+1} - \bar{\mathbf{G}}\mathbf{d}^{n+1}, \quad (38)$$

$$\mathbf{S}\dot{\mathbf{p}}^{n+1} = \tilde{\mathbf{F}}^{\text{ext}} - \tilde{\mathbf{F}}^{\text{int}} - \bar{\mathbf{Q}}\mathbf{d}^{n+1} - \mathbf{Q}\mathbf{p}^{n+1}. \quad (39)$$

Above, a mass proportional damping matrix \mathbf{C} can be introduced if desired. Similar to Section 4.2, the matrices associated with the time rate change of the semi-Lagrangian kernels, \mathbf{G} , $\bar{\mathbf{G}}$, $\tilde{\mathbf{G}}$, and $\tilde{\mathbf{G}}$, can be omitted for computational efficiency. Subsequently, equations (38) and (39) degenerate to

$$(\mathbf{M} + 0.5\Delta t\mathbf{C})\mathbf{a}^{n+1} = \mathbf{F}^{\text{ext}} - \mathbf{F}^{\text{int}} - \mathbf{C}\hat{\mathbf{v}}^{n+1}, \quad (40)$$

$$\mathbf{S}\dot{\mathbf{p}}^{n+1} = \tilde{\mathbf{F}}^{\text{ext}} - \tilde{\mathbf{F}}^{\text{int}}. \quad (41)$$

The lumped matrix scheme by the row sum is employed for \mathbf{M} and \mathbf{S} to acquire diagonal matrices. This process leads to an explicit scheme, the information of at the $(n+1)$ -th time step is fully independent on the information from the n -th time step, and therefore it is efficient for highly dynamic applications. However, the scheme is conditionally stable. The stable time step size can be estimated using the von Neumann method and the details are referred to (Chi and Siriaksorn, 2017).

4.1.4. Domain integration in the Galerkin formulation

The domain integration in the meshfree Galerkin formulation (equations (7) and (24)-(25)) requires special attention due to the nature of the RK approximation and the applications involving extreme deformation and discontinuities (Chen et al. 2013; Hillman et al., 2014; Chen et al. 2017). In this project, the Modified Stabilized Nonconforming Nodal Integration (MSNNI) is implemented (Chen et al., 2006). The direct gradients involved in equations (12)-(16) and (32)-(37) are replaced by an assumed gradient operator to construct smoothed derivatives of the shape function over a prismatic nodal representative domain (Figure 2), that is

$$\bar{\nabla} \Psi_I(\mathbf{x}_L) = \frac{1}{V_L} \int_{\Gamma_L} \Psi_I(\mathbf{x}) \mathbf{n}(\mathbf{x}) d\Gamma \quad (42)$$

where V_L and Γ_L are the volume and boundary, respectively, of the nodal representative domain of node L and \mathbf{n} is the unit outward normal vector of Γ_L . Therefore, the smoothed strain field and pressure gradient field can be constructed as:

$$\bar{\boldsymbol{\varepsilon}}^h(\mathbf{x}_L) = \sum_{I=1}^{NP} \bar{\mathbf{B}}_I(\mathbf{x}_L) \mathbf{d}_I, \quad (43)$$

$$\bar{\nabla} \mathbf{P}^h(\mathbf{x}_L) = \sum_{I=1}^{NP} \bar{\mathbf{B}}_I^p(\mathbf{x}_L) p_I. \quad (44)$$

The detailed formulation of $\bar{\mathbf{B}}_I$ and $\bar{\mathbf{B}}_I^p$ is referred to (Siriaksorn et al., 2017). The matrices on the right hand side of equations (38) and (41) after applying equations (43) and (44) are summarized as follows.

$$\left. \begin{aligned} \mathbf{F}_I^{\text{ext}} &= \sum_{K=1}^{NP} \Psi_I(\mathbf{x}_K) \mathbf{h}(\mathbf{x}_K) A_K, \\ \bar{\mathbf{F}}_I^{\text{int}} &= \sum_{L=1}^{NP} \bar{\mathbf{B}}_I^T(\mathbf{x}_L) \bar{\boldsymbol{\sigma}}(\mathbf{x}_L) V_L - \sum_{L=1}^{NP} \bar{\mathbf{B}}_I^T(\mathbf{x}_L) \alpha \Psi_J(\mathbf{x}_L) V_L p_J^{n+1} - \sum_{L=1}^{NP} \Psi_I(\mathbf{x}_L) \mathbf{b}(\mathbf{x}_L) V_L, \\ \tilde{\mathbf{F}}_I^{\text{ext}} &= \sum_{K=1}^{NP} \Psi_I(\mathbf{x}_K) v_s(\mathbf{x}_K) A_K, \\ \tilde{\mathbf{F}}_I^{\text{int}} &= \sum_{L=1}^{NP} \Psi_I(\mathbf{x}_L) \alpha \bar{\mathbf{B}}_J(\mathbf{x}_L) V_L \mathbf{v}_J^{n+1} + \sum_{L=1}^{NP} (\bar{\mathbf{B}}_I^p)^T(\mathbf{x}_L) \frac{k}{\mu} \bar{\mathbf{B}}_J^p(\mathbf{x}_L) V_L p_J^{n+1} - \sum_{L=1}^{NP} (\bar{\mathbf{B}}_I^p)^T(\mathbf{x}_L) \frac{k}{\mu} \rho^f \mathbf{g} V_L \end{aligned} \right\} (45)$$

where A_K denotes the boundary surface area of nodal domain K . To further enhance the stability, the terms

$$w \sum_{L=1}^{NP} \sum_{\xi=1}^{Ns_L} (\bar{\mathbf{B}}_I(\mathbf{x}_L) - \bar{\mathbf{B}}_I(\mathbf{x}_\xi))^T \mathbf{E} (\bar{\mathbf{B}}_J(\mathbf{x}_L) - \bar{\mathbf{B}}_J(\mathbf{x}_\xi)) V_\xi \mathbf{d}_J^{n+1} \quad (46)$$

and

$$w^p \sum_{L=1}^{NP} \sum_{\xi=1}^{Ns_L} (\bar{\mathbf{B}}_I^p(\mathbf{x}_L) - \bar{\mathbf{B}}_I^p(\mathbf{x}_\xi))^T \frac{k}{\mu} (\bar{\mathbf{B}}_J^p(\mathbf{x}_L) - \bar{\mathbf{B}}_J^p(\mathbf{x}_\xi)) V_\xi p_J^{n+1} \quad (47)$$

are added in $\mathbf{F}_I^{\text{int}}$ and $\tilde{\mathbf{F}}_I^{\text{int}}$, respectively, in equation (45), and the terms

$$w \sum_{L=1}^{NP} \sum_{\xi=1}^{Ns_L} (\bar{\mathbf{B}}_I(\mathbf{x}_L) - \bar{\mathbf{B}}_I(\mathbf{x}_\xi))^T \mathbf{E} (\bar{\mathbf{B}}_J(\mathbf{x}_L) - \bar{\mathbf{B}}_J(\mathbf{x}_\xi)) V_\xi \quad (48)$$

$$w^p \sum_{L=1}^{NP} \sum_{\xi=1}^{Ns_L} (\bar{\mathbf{B}}_I^p(\mathbf{x}_L) - \bar{\mathbf{B}}_I^p(\mathbf{x}_\xi))^T \frac{k}{\mu} (\bar{\mathbf{B}}_J^p(\mathbf{x}_L) - \bar{\mathbf{B}}_J^p(\mathbf{x}_\xi)) V_\xi \quad (49)$$

are added in \mathbf{M} and \mathbf{S} , respectively, in equations (40) and (41). Above w and w^p are stabilization parameters ranging between 0 and 1, \mathbf{E} is the elastic part of the material tangent tensor, V_c is the nodal volume associated with subdomain j (see Figure 2), $\sum_{\xi=1}^{Ns_L} V_\xi = V_L$, and Ns_L is the number of subdomains in the nodal representative domain of node L . The details are referred to (Siriaksorn et al., 2017).

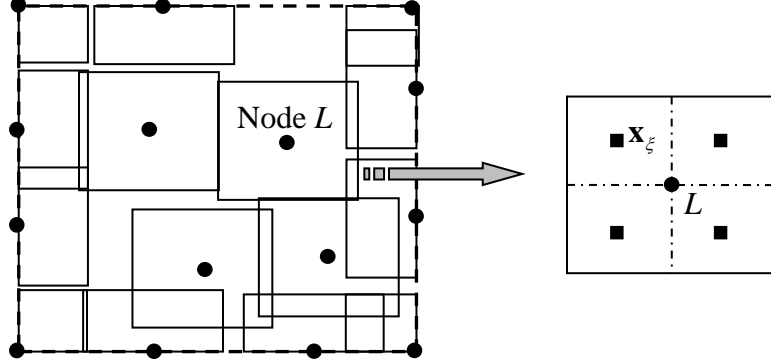


Figure 2. Nodal smoothing domain for the modified stabilized nonconforming nodal integration

4.2. Soil constitutive models

The effective stress $\bar{\sigma}$ described in Section 4.1.3 is decoupled from the fluid phase. It can be computed using solid constitutive models independent of the fluid phase. Several features are necessary to accurately capture the soil behavior in the deformation under penetration. The ability to capture large deformation hardening and softening is paramount. The ability to capture the transition from dilation to compaction, tensile behavior, rate dependence, and triaxiality of the stress state can also be important. In this project, two constitutive models are developed and implemented to represent soil behaviors.

4.2.1. Non-associated Drucker-Prager with damage model

The Drucker-Prager yield function is described as

$$F_{DP} = \sqrt{2J_2} + \beta p - A \quad (50)$$

where J_2 is the second invariant of the deviatoric part of $\hat{\sigma}$; p is one-third of the trace of $\hat{\sigma}$; β and A are material parameters; $\hat{\sigma}$ is the effective stress before degraded by material damage. The Drucker-Prager material parameters β and A are related to cohesion c and friction angle ϕ of Mohr-Coulomb by

$$\beta = \frac{2\sqrt{6}\sin\phi}{3-\sin\phi}, \quad (51)$$

$$A = \frac{2\sqrt{6}c\cos\phi}{3-\sin\phi}. \quad (52)$$

Considering a non-associated flow rule, in this project the plastic potential function takes the following form

$$G = \sqrt{2J_2} + bp - A \quad (53)$$

where b can be related to the dilatancy angle ψ as

$$b = \frac{2\sqrt{6} \sin \psi}{3 - \sin \psi}. \quad (54)$$

A damage parameter d is introduced to degrade the deviatoric part and the tensile volumetric part of the effective stress $\hat{\sigma}$. It yields the total (damaged) effective stress $\bar{\sigma}$ as

$$\bar{\sigma} = \hat{\sigma}^{dev} (1-d) + ((1-d)tr\hat{\sigma}^+ + tr\hat{\sigma}^-) \mathbf{I} \quad (55)$$

where superscripts dev , $+$, and $-$ indicate deviatoric, tensile, and compressive parts of the corresponding terms, respectively. A linear evolution of the damage parameter d is assumed:

$$d = \frac{c_1(\eta - c_2)}{\eta(c_1 - c_2)} ; \quad \eta \geq c_2 \quad (56)$$

where η is the norm of the deviatoric strain (i.e., $\eta = \sqrt{\mathbf{\epsilon}^{dev} : \mathbf{\epsilon}^{dev}}$) used as a means to measure material damage. The parameter c_2 specifies the initiation point, when material starts to degrade ($d = 0$). The parameter c_1 specifies the critical point, when material is fully damaged ($d = 1$).

4.2.2. Three-invariant Soil Constitutive Model

To capture the transition from dilation to compaction, tensile behavior, rate dependence, and triaxiality of the stress state, a three-invariant continuum cap plasticity model is developed for large deformation of soil in penetration problems. This model is capable of simulating multiple failure mechanisms including loss of strength under tension and combined shear and compaction yielding. It features a nonlinear pressure-dependent shear yield surface as well as a cap surface governing inelastic compaction hardening which is formulated as an explicit expression of porosity. It also accounts for the differences in triaxial extension and compression strength. Adapted from the previously developed Sandia GeoModel (Fossum and Brannon, 2004b), the shear and tension surfaces are simplified using a hyperbolic function which promises a less computationally expensive constitutive model.

Dynamic problems and systems exposed to high strain rates, e.g. soil penetration problems, are examples where addressing the rate-dependency factor plays a key role in analyzing and predicting the system response. Here, viscoplastic regularization by using an overstress model of the Duvaut-Lions type is adopted in order to capture such rate dependency of the soil constitutive behavior (Duvaut and Lions, 1972). Viscoplasticity also serves to regularize the constitutive model (Simo and Hughes, 1998). Therefore, it can be used as a remedy for loss of ellipticity issues arising from softening or nonassociativity.

4.2.2.1. Yield surface

An elliptical tension cap to better capture the tensile behavior was added to the yield surface in (Motamedi and Foster, 2015). In this work modeling, the shear and tension surfaces are simplified using a hyperbolic formulation adapted from (Carol et al., 1997). While they used the hyperbolic surface for yielding along a discrete surface, the same concepts can be adjusted for use in a continuum yield surface.

The shear yield surface is given as

$$F_f = \sqrt{(C - MI_1)^2 - (C - M\Xi)^2} \quad (57)$$

where I_1 is the first invariant of $\bar{\sigma}$, Ξ measures the maximum elastic value of I_1 , C is a shear strengthen face parameter, and M is the tangential slope of the shear yield surface in meridional stress space (see Figure 3). M is treated as constant, but the other two parameters may vary.

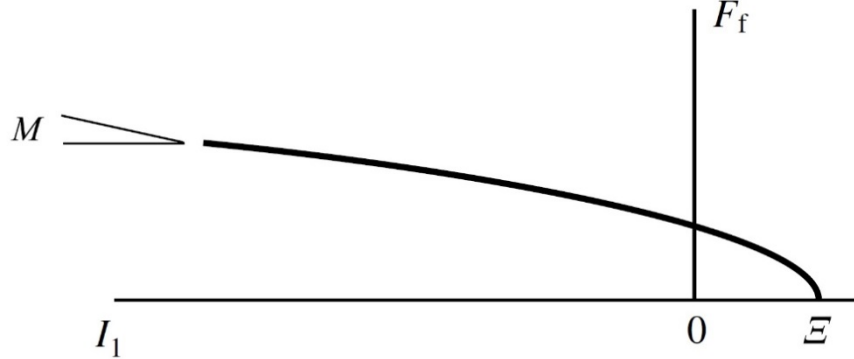


Figure 3. Shear failure surface F_f

This yield surface is modified by an elliptical cap function F_c

$$F_c(I_1) = 1 - H(\kappa - I_1) \left(\frac{I_1 - \kappa}{X - \kappa} \right)^2 \quad (58)$$

where

$$X(\kappa) = \kappa - RF_f(\kappa) \quad (59)$$

is the value of I_1 where hydrostatic compression occurs, $H(x)$ is the Heaviside function, and R is a material parameter that controls the aspect ratio of the cap.

The entire yield surface may be written as

$$f = \Gamma(\beta) \sqrt{J_2} - \sqrt{F_c F_f} \quad (60)$$

where Γ is a modifying function which is introduced to capture the difference between triaxial extension and compression strength (Fossum and Brannon, 2004b; Foster et al., 2005). Thus far, we have implemented the Gudehus form of the modifying function (Gudehus, 1973):

$$\begin{aligned}\Gamma(\beta) &= \frac{1}{2} \left(1 + \sin 3\beta + \frac{1}{\psi} (1 - \sin 3\beta) \right) \\ &= \frac{1}{2} \left(1 - \frac{3\sqrt{3}J_3}{2(J_2)^{3/2}} + \frac{1}{\psi} \left(1 + \frac{3\sqrt{3}J_3}{2(J_2)^{3/2}} \right) \right)\end{aligned}\quad (61)$$

where ψ is the constant ratio triaxial extension and compression strength.

4.2.2.2. Evolution of plastic variables

(a) Shear and tensile parameters

The evolution of C and Ξ follow a hardening and softening function. These strength parameters may evolve differently depending on whether the loading is compressive or tensile, and how much shear is involved. Hence we introduce a parameter γ to describe the evolution

$$\dot{\gamma} = a_t \langle \dot{\delta}_v^p \rangle + a_c \langle -\dot{\delta}_v^p \rangle + a_s \|\dot{\epsilon}^p\| \quad (62)$$

$$\gamma = \int \dot{\gamma} dt \quad (63)$$

where a_t , a_c , and a_s are material constants. The terms $\dot{\delta}_v^p$ and $\|\dot{\epsilon}^p\|$ represent the volumetric part of the plastic strain rate and norm of the deviatoric part of the plastic strain rate, respectively, and $\langle \bullet \rangle$ are Macaulay brackets. Hence, $\dot{\gamma}$ is related to the plastic multiplier λ , but weighted for the type of deformation. For the evolution of the variables C and Ξ , we propose a hardening evolution following a normal function

$$C(\gamma) = (C_{max} - C_{res}) e^{-b_C(\gamma-\gamma_C)^2} + C_{res} \quad (64)$$

$$\Xi(\gamma) = (\Xi_{max} - \Xi_{res}) e^{-b_\Xi(\gamma-\gamma_\Xi)^2} + \Xi_{res} \quad (65)$$

Here, the maximum value of the parameter is C_{max} or Ξ_{max} , and residual values C_{res} or Ξ_{res} are proposed. These values are allowed due to small amounts of shear and tensile strength due to interlocking effects even in granular materials, although the values may be set to zero. The material constants γ_C and γ_Ξ indicate the values of γ where peak strength is reached, and b_C and b_Ξ are related to the initial values of the parameters C_0 and Ξ_0 by the formula

$$b_C = \frac{1}{\gamma_C^2} \ln \left(\frac{C_{max} - C_{res}}{C_0 - C_{res}} \right) \quad (66)$$

$$b_\Xi = \frac{1}{\gamma_\Xi^2} \ln \left(\frac{\Xi_{max} - \Xi_{res}}{\Xi_0 - \Xi_{res}} \right) \quad (67)$$

The parameters can be adjusted so that this function predicts hardening and softening, ductile softening, or brittle softening depending on the parameter choices. These functions are shown in Figure 4.

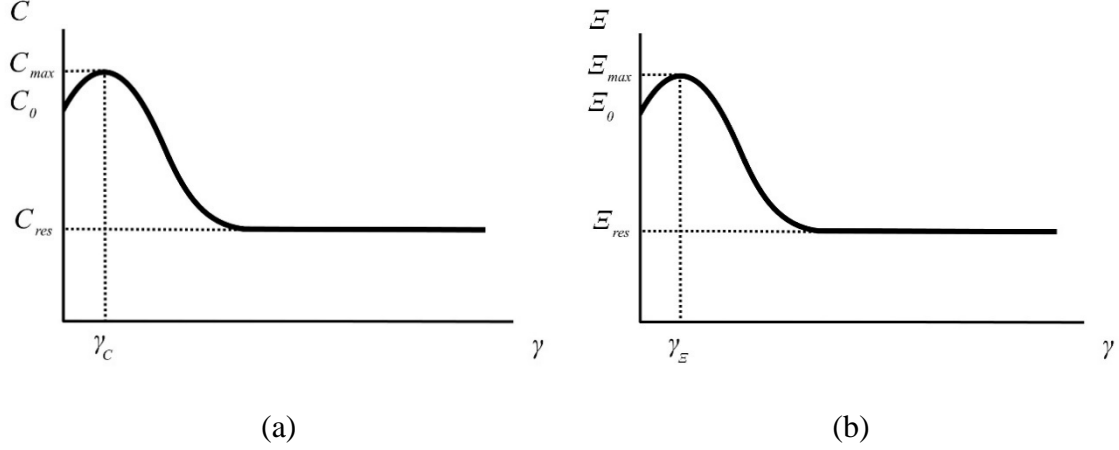


Figure 4. Evolution of C with respect to γ , (b) Evolution of Ξ with respect to γ .

(b) Cap parameter

The cap parameter κ is assumed, as in earlier work, to be a function only of the volumetric strain. The evolution of this variable is related to pore collapse, grain crushing, and other micromechanical phenomena. In order to couple this model in a poromechanical framework, where permeability changes with porosity, we need to track the changing porosity of the soil. Therefore, we reformulate the plastic volumetric deformation as an explicit expression of the porosity.

In small strain, it can be shown that the void ratio n is related to volumetric strain $\dot{\phi}_v$ by the formula

$$\dot{\phi}_v = \frac{n - n_0}{1 - n} \quad (68)$$

where n_0 is the initial void ratio. Similarly, the unloaded porosity (the recovered porosity of the material after elastic unloading) n^* is related to the *plastic* volumetric strain as

$$\dot{\phi}_v^p = \frac{n^* - n_0^*}{1 - n^*} \quad (69)$$

In large deformation, with $\dot{\phi}$ as the Eulerian logarithmic (Hencky) strain, the formula becomes

$$\dot{\phi}_v^p = \ln\left(\frac{1 - n_0^*}{1 - n^*}\right) \quad (70)$$

We propose a hydrostatic “crush curve” in the $I_1 - n^*$ plane as

$$n^* = n_0^* \exp\left[q_l(X - X_0)\right] \quad (71)$$

where q_l is a material constant. Hence as I_1 achieves negative large values, all the pore space approaches zero. This model may have issues with conditioning if the porosity becomes very small, and a second factor similar to that proposed by (Fossum and Brannon, 2004a) may improve the transition from compaction to dilation.

Recall that

$$X(\kappa) := \kappa - RF_f^g(\kappa) \quad (72)$$

Hence, we can track the evolution of κ as

$$\dot{\kappa} = \frac{\partial \kappa}{\partial X} \frac{\partial X}{\partial n^*} \frac{\partial n^*}{\partial \dot{\phi}_v^p} \dot{\phi}_v^p = \frac{3\dot{\gamma} \frac{\partial g}{\partial I_1}}{\frac{\partial \dot{\phi}_v^p}{\partial n^*} \frac{\partial n^*}{\partial X} \frac{\partial X}{\partial \kappa}} \quad (73)$$

It can easily be shown that

$$\frac{\partial \dot{\phi}_v^p}{\partial n^*} = \frac{1 - n_0^*}{(1 - n^*)^2} \quad (74)$$

$$\frac{\partial n^*}{\partial X} = q n_0^* \exp\left[q_l(X - X_0)\right] \quad (75)$$

$$\frac{\partial X}{\partial \kappa} = 1 - R \frac{\partial F_f^g(\kappa)}{\partial \kappa} \quad (76)$$

4.2.2.3. Plastic potential

For most geomaterials, a plastic potential function separate from yield function is necessary to prevent the overprediction of plastic volumetric strain. On shear surface, the parameter M has the greatest influence on the volumetric dilation, and replacing this with a smaller M_g will reduce the dilation on the shear surface. We also replace C with C_g defined by

$$C_g(\gamma) = (C_{maxg} - C_{resg}) e^{-b_c(\gamma - \gamma_c)^2} + C_{resg} \quad (77)$$

with the modified constants C_{maxg} , C_{resg} , C_{0g} , and γ_{Cg} .

The plastic potential g is modified from the yield function

$$g = \Gamma(\beta) \sqrt{J_2} - \sqrt{F_c^g} F_f^g \quad (78)$$

where

$$F_f^g = \sqrt{\left(C_g - M_g I_1\right)^2 - \left(C_g - M_g \Xi\right)^2} \quad (79)$$

$$F_c^g = 1 - H(\kappa - I_1) \left(\frac{I_1 - \kappa}{X - \kappa} \right)^2 \quad (80)$$

Nonassociativity on the cap follows (Regueiro and Foster, 2011), where

$$X_g(\kappa) = \kappa - R_g F_f^g(\kappa) \quad (81)$$

4.2.2.4. Numerical implementation

Numerically, the RKPM code uses a finite difference scheme for time integration, evaluating the variables at a finite number of discrete points in time. At the integration point, the problem is strain driven. Hence, given the values of the stress and internal state variables, κ and γ at time t_n , along with the strain $\dot{\mathbf{o}}_{n+1}$ at the current time t_{n+1} , we aim to find the updated values of these parameters at time t_{n+1} . In plasticity formulations, this is typically solved using a return mapping algorithm. In this case, the equations are integrated using an implicit or backward Euler approximation which brings first-order accuracy as well as unconditional stability (at the integration point level). First a trial stress σ_{n+1}^{tr} is computed assuming that the step will be elastic

$$\sigma_{n+1}^{\text{tr}} = \sigma_n + \mathbf{C}^e : \Delta \dot{\mathbf{o}} \quad (82)$$

If the yield surface is violated, then the return mapping algorithm is invoked to return the stress to the yield surface and account for its evolution.

Also, we employ spectral decomposition of the stress, as used in (Borja et al., 2003; Foster et al., 2005; Tamagnini et al., 2002). This technique helps to reduce the number of unknowns by working on the principal stresses rather than the full effective stress tensor. Because the principal directions, or Eigenvectors, of the stress are identical in the trial and final states for isotropic plasticity models, we can determine the directions from the trial state and only solve for the principal stresses, or Eigenvalues. Adding the other independent unknowns, the internal state variables and the plastic multiplier, the vector of unknowns that should be solved for at time t_{n+1} takes the form

$$\mathbf{X} = \left\{ \sigma_I^{\text{corr}} \quad \sigma_{II}^{\text{corr}} \quad \sigma_{III}^{\text{corr}} \quad \Delta\kappa \quad \Delta\gamma \quad \Delta\lambda \right\}^T \quad (83)$$

where σ_A^{corr} are plastic correctors for the stress

$$\sigma_A^{\text{corr}} = \sigma_A - \sigma_A^{\text{tr}} \quad (84)$$

We solve this system by using a standard Newton-Raphson algorithm. When adopting an N-R algorithm, the iterative calculation results

$$\mathbf{X}_{n+1}^{k+1} = \mathbf{X}_{n+1}^k - \left[\left(\frac{\mathbf{D}\mathbf{R}}{\mathbf{D}\mathbf{X}} \right)_{n+1}^k \right]^{-1} \mathbf{R}_{n+1}^k \quad (85)$$

where $k+1$ denotes the current iteration number. The residual vector for this problem takes the form

$$\mathbf{R}(\mathbf{X}) = \begin{Bmatrix} \Delta\lambda a_{1A}^e \left(\frac{\partial g}{\partial \sigma_A} \right) + \sigma_I^{\text{corr}} \\ \Delta\lambda a_{2A}^e \left(\frac{\partial g}{\partial \sigma_A} \right) + \sigma_{II}^{\text{corr}} \\ \Delta\lambda a_{3A}^e \left(\frac{\partial g}{\partial \sigma_A} \right) + \sigma_{III}^{\text{corr}} \\ \Delta\lambda h^\kappa - \Delta\kappa \\ (a_t \dot{\sigma}_v^p + a_c - \dot{\sigma}_v^p + a_s \dot{\epsilon}^p) - \Delta\gamma \\ f \end{Bmatrix} = 0 \quad (86)$$

where g denotes the plastic potential function. The subscript $n+1$ is omitted in the above equations to simplify notation. The summation convention is also used in the first three equations. The tensor \mathbf{a}^e is the elasticity tensor projected to principal stress space and has the form

$$\mathbf{a}^e = \begin{bmatrix} \lambda + 2\mu & \lambda & \lambda \\ \lambda & \lambda + 2\mu & \lambda \\ \lambda & \lambda & \lambda + 2\mu \end{bmatrix} \quad (87)$$

where λ and μ are Lamé's first and second constants, respectively.

The return mapping algorithm then takes the form as outlined in Box 4.1.

Box 4.1: Summary of the return mapping algorithm.

<i>Step 1.</i>	Compute $\sigma_{n+1}^{\text{tr}} = \sigma_n + C^e : \Delta\dot{\sigma}$.
<i>Step 2.</i>	Spectrally decompose $\sigma_{n+1}^{\text{tr}} = \sum_{A=1}^3 \sigma_A^{\text{tr}} \mathbf{m}^{(A)}$.
<i>Step 3.</i>	Check yielding: is $f > 0$? If no, set $\sigma_{n+1} = \sigma_{n+1}^{\text{tr}}$ and exit.
<i>Step 4.</i>	Set $X_0 = 0$ and iterate following Eq. 4.31 until the relative convergence tolerance is met.
<i>Step 5.</i>	Update: $\sigma_{n+1} = \sigma_{n+1}^{\text{tr}} + \sum_{A=1}^3 \sigma_A^{\text{corr}} \mathbf{m}^{(A)}$ $\kappa_{n+1} = \kappa_n + \Delta\kappa$ $\gamma_{n+1} = \gamma_n + \Delta\gamma$ and exit.

4.2.2.5. Parameter fitting

A fitting procedure for the three-invariant model based on standard geotechnical tests is given in (Fossum and Brannon, 2004a). The procedure will be largely the same, though the forms of the functions to be fit are different. With regards to the yield surface, an additional tensile test will be necessary to accurately fit the parameter Ξ .

The hardening/softening functions can still be fit using, say, triaxial test data, but there will be a few more parameters to tune during the process. However, some, such as γ_c and γ_Ξ , will have fairly apparent values, making them easier to fit.

5. Results and Discussion

5.1. Verifications

The three-invariant soil constitutive model, discussed in Section 4.2, is first implemented within an FEM code. Using the three-invariant model and adopting a specific set of material constants and ignoring the cap, we are able to recover a non-associative Drucker-Prager plasticity model with zero hardening/softening. We used this characteristics of the model to verify the shear surface implementation, of the three-invariant model using a number of Drucker-Prager benchmark tests.

The model is also implemented within the mesh-free code. The two implementations, FEM and mesh-free, are then compared by performing a number of simulations, including the uniaxial and triaxial compression, uniaxial tension, and combined compression-shear tests, on an 8-node test model. For FEM simulations, a 3D solid cubic finite element with eight nodes and eight integration points is employed. It should also be noted that the employed FEM framework uses small strain formulations while the mesh-free code can handle large deformations and rotations.

The two frameworks, FEM and mesh-free, are also compared for the uniaxial and triaxial compression tests using a Drucker-Prager model with linear hardening/softening. Hence, as for the constitutive model, two cases are considered: a non-associative Drucker-Prager plasticity model with linear evolution in the cohesive strength parameter, and the three-invariant cap plasticity model regularized by the Duvaut-Lions viscoplasticity model. The results are discussed in the following sections.

5.1.1. Uniaxial compression test

The first example, in FEM, consists of a one-element model under uniaxial compression, as shown in Figure 5. The mesh-free simulation is modeled using 8 nodes in order to best reproduce the behavior of the FEM implementation. In order to impose the uniaxial compressive strain, a displacement-controlled approach is carried out by applying $d = 0.02$ mm downward prescribed displacement on the top side of the model, i.e., the top four nodes.

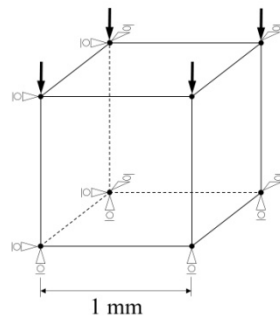


Figure 5. Uniaxial compression test. Dimensions, loading, and boundary conditions.

As for the constitutive model, a non-associative Drucker-Prager plasticity model with linear evolution in the cohesive strength parameter is used first. The material properties are shown in Table 1.

Table 1. Material properties for the Drucker-Prager uniaxial compression test.

Parameter	Symbol	Value
Young's modulus	E	72 MPa
Poisson's ratio	ν	0.44
Drucker-Prager material constant	A	0.25 MPa
Drucker-Prager material constant	β	0.05
Drucker-Prager material constant	b	0.025
Hardening/softening modulus	H^α	25 MPa

For the Drucker-Prager criterion employed here, the yield function is expressed as

$$f = \sqrt{2 J_2} - (A - \beta p) \quad (88)$$

where J_2 is the second deviatoric stress invariant, α , cohesion-like parameter, β , friction-like parameter, and p denotes the mean normal stress defined as

$$p = \text{tr}(\boldsymbol{\sigma})/3 \quad (89)$$

with $\boldsymbol{\sigma}$ being the Cauchy stress tensor and $\text{tr}(\bullet)$ for the trace operator. A plastic potential function is also used of the form

$$g = \sqrt{2 J_2} - (A - bp) \quad (90)$$

where b is the dilation constant. The hardening/softening modulus is used to demonstrate the evolution in A as

$$\dot{A} = H^\alpha \dot{\lambda} \quad (91)$$

hence, forming a linear hardening/softening evolution. The parameter $\dot{\lambda}$ represents the value of the plastic strain rate.

The axial stress-strain responses for the two frameworks are plotted in Figure 6. A good agreement is observed comparing the two graphs.

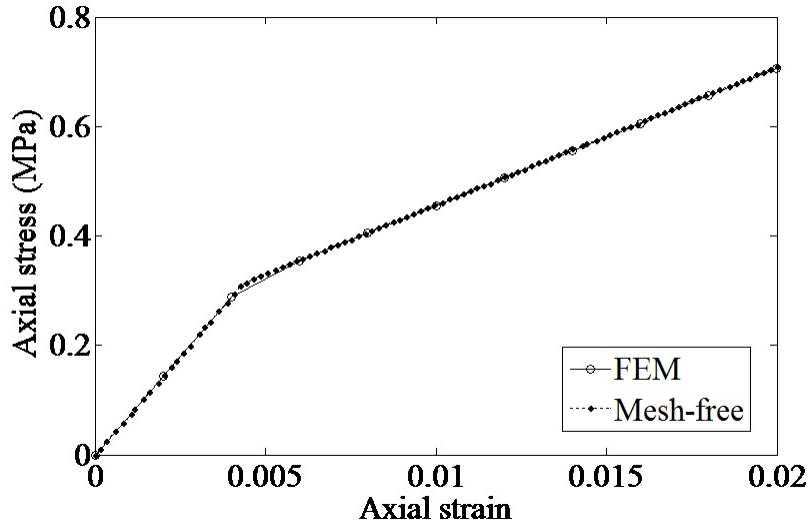


Figure 6. Drucker-Prager and uniaxial compression test. Compressive axial stress vs. compressive axial strain response for FEM and mesh-free.

For this test, the three-invariant plasticity model is also adopted where the material constants are shown in Table 2. The two frameworks give similar stress-strain responses, as shown in Figure 6.

Table 2. Material properties for the three-invariant plasticity uniaxial compression test.

Symbol	Value
E	9000.0 MPa
ν	0.15
ψ	0.8
R	1.0
R_g	1.0
κ_0	-50.0 MPa
M	0.2
M_g	0.2
a_t	100.0
a_c	100.0
a_s	50.0
C_{max}	5.5 MPa
C_{maxg}	5.5 MPa
Ξ_{max}	11.0 MPa
C_{res}	2.0 MPa
C_{resg}	2.0 MPa
Ξ_{res}	7.0 MPa
γ_C	1.0
γ_{Cg}	1.0
γ_Ξ	1.0
C_0	4.5 MPa
C_{0g}	4.5 MPa
Ξ_0	10.0 MPa
n_0	1.0e-3
n_0^*	1.0e-3
q_1	1.0
τ	0.01

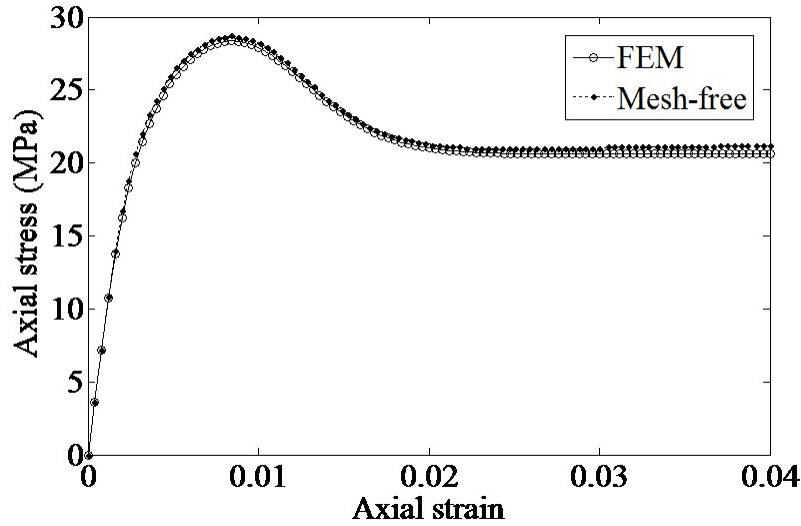


Figure 7. Three-invariant plasticity and uniaxial compression test. Compressive axial stress vs. compressive axial strain for FEM and mesh-free.

5.1.2. Triaxial compression test

The second example, in FEM, consists of a one-element model under triaxial compression, as shown in Figure 7. Again, the mesh-free simulation is modeled using 8 nodes. The triaxial test, in general, is one of the most common and widely performed laboratory experiments, allowing to measure the mechanical properties of soil, rock, and other granular materials for use in engineering design. These material properties include the angle of shearing resistance, apparent cohesion, and dilatancy angle among others. The material properties for the Drucker-Prager test are shown in Table 3 and the parameters have the same meanings as in Section 5.1.2.1.

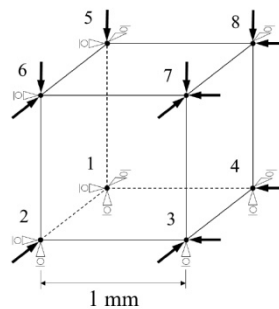


Figure 8. Triaxial compression test. Dimensions, loading, and boundary conditions.

Table 3. Material properties for the Drucker-Prager triaxial compression test.

Parameter	Symbol	Value
Young's modulus	E	9000.0 MPa
Poisson's ratio	ν	0.15
Drucker-Prager material constant	A	8.034 MPa
Drucker-Prager material constant	β	0.633
Drucker-Prager material constant	b	0.3165
Hardening/softening modulus	H^α	-100.0 MPa

In order to model a triaxial compression test, a given pressure should be applied to all sides of the model. A continued displacement or load is then applied in one direction, maintaining the pressure on the other sides. Here, imposing the triaxial compressive strain is conducted by using a displacement-controlled approach where a prescribed displacement is applied on the sides of the element, as shown in Figure 7.

The model is initially loaded at a strain rate of 0.0004 per second on all sides for one second. This applies a confining stress on the model similar to what is done by pressurizing the cell fluid surrounding the specimen in a laboratory experiment. The strain rate is then instantaneously dropped to 0 and held constant for another second. Then, the rate is raised to 0.0008 per second only in one direction (imposed on the top side) for the rest of the simulation. Strain rate change through the 5-second simulation and the associated imposed displacement, d , at each time step are plotted in Figure 8a and Figure 8b, respectively. The axial stress-strain responses are depicted in Figure 9 where the graphs are fairly analogous.

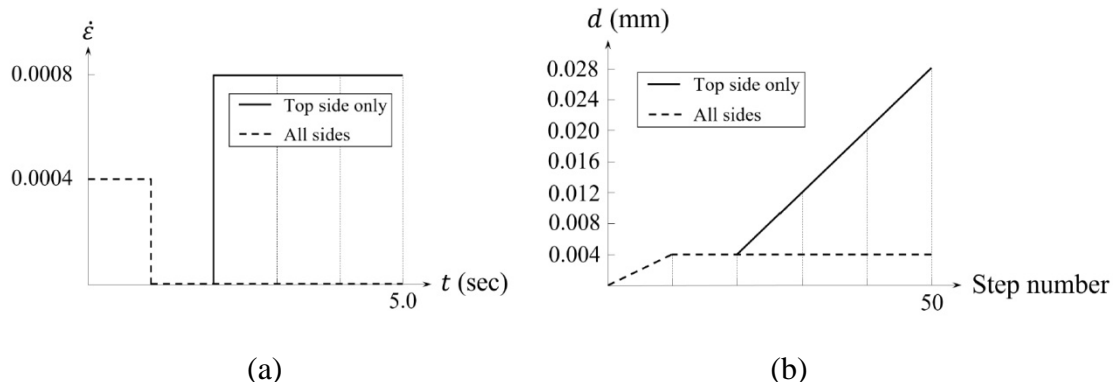


Figure 9. Drucker-Prager and triaxial compression test. (a) Strain rate vs. time, (b) Imposed displacement vs. step number.

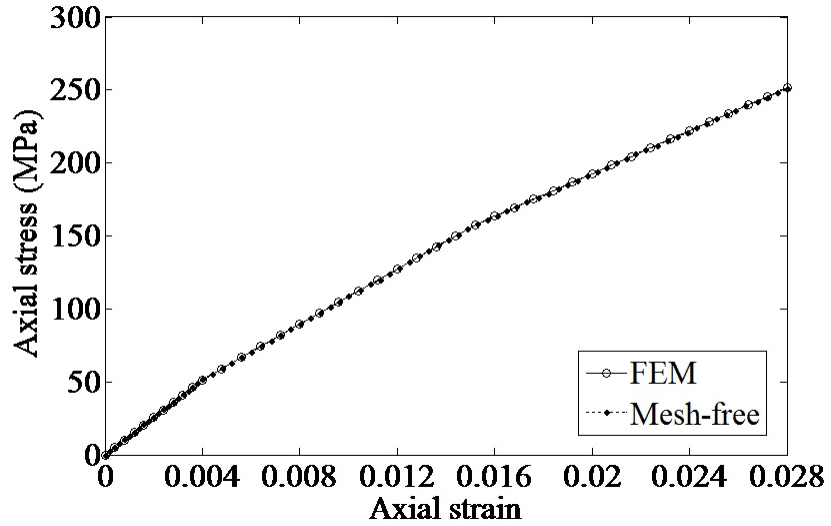


Figure 10. Drucker-Prager and triaxial compression test. Compressive axial stress vs. compressive axial strain.

The three-invariant plasticity model is also adopted where the material constants are shown in Table 4. For this model, the loading conditions are modified as an imposed displacement of $d = 0.0015$ mm on all sides for the first second following a relaxation step for another second. Then, a displacement of $d = 0.02$ mm is applied only in one direction (imposed on the top side) for the rest of the simulation. The total simulation time is 3 seconds. The axial stress-strain responses are plotted in Figure 10. A similar response is observed.

Table 4. Material properties for the three-invariant plasticity triaxial compression test.

Symbol	Value
E	9000.0 MPa
ν	0.15
ψ	0.8
R	2.0
R_g	2.0
κ_0	-50.0 MPa
M	0.2
M_g	0.2
a_t	100.0
a_c	100.0
a_s	50.0
C_{max}	5.5 MPa
C_{maxg}	5.5 MPa
Ξ_{max}	11.0 MPa
C_{res}	2.0 MPa
C_{resg}	2.0 MPa
Ξ_{res}	7.0 MPa
γ_C	1.0
γ_{Cg}	1.0
γ_Ξ	1.0
C_0	4.5 MPa
C_{0g}	4.5 MPa
Ξ_0	10.0 MPa
n_0	1.0e-1
n_0^*	1.0e-1
q_1	10.0
τ	0.01

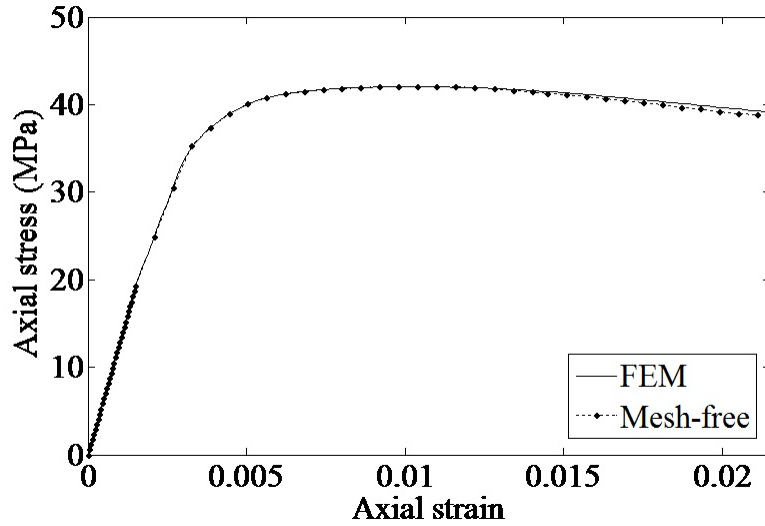


Figure 11. Three-invariant plasticity and triaxial compression test. Compressive axial stress vs. compressive axial strain.

5.1.3. Uniaxial extension test

The next two simulations are only performed using the three-invariant model. This example, in FEM, consists of a one-element model under uniaxial extension, as shown in Figure 11. The mesh-free simulation is modeled using 8 nodes as before. By performing this test, we aim to check the tension cap of the model. In order to impose the uniaxial tensile strain, a displacement-controlled approach is carried out by applying $d = 0.01$ mm upward prescribed displacement on the top side of the model, i.e., the top four nodes.

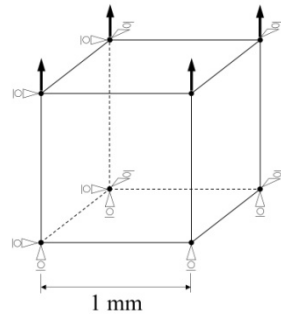


Figure 12. Uniaxial extension test. Dimensions, loading, and boundary conditions.

The material constants for the three-invariant model are identical to those in Table 2, for uniaxial compression test, except for $M_g = 0.05$ which is chosen in order to test nonassociativity. Figure 12 compares the axial stress-strain responses for the two frameworks. The graphs are comparable.

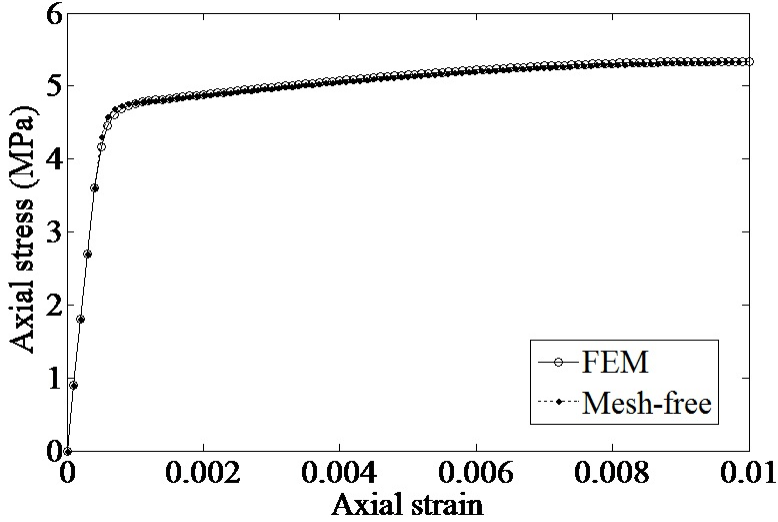


Figure 13. Three-invariant plasticity and uniaxial extension test. Axial stress vs. axial strain for FEM and mesh-free.

5.1.4. Combined compression-shear test

The last simulation includes a compression step followed by a shear loading mainly to verify the model under a rotation of the principal stress axes. Figures 13a and Figure 13b provide the loading and boundary conditions of the two steps. During compression, a displacement-controlled approach is carried out by applying $d_c = 0.01$ mm downward prescribed displacement on the top side of the model. Next, the top face is constrained to move in vertical direction, and the top four nodes are moved horizontally by applying $d_s = 0.02$ mm.

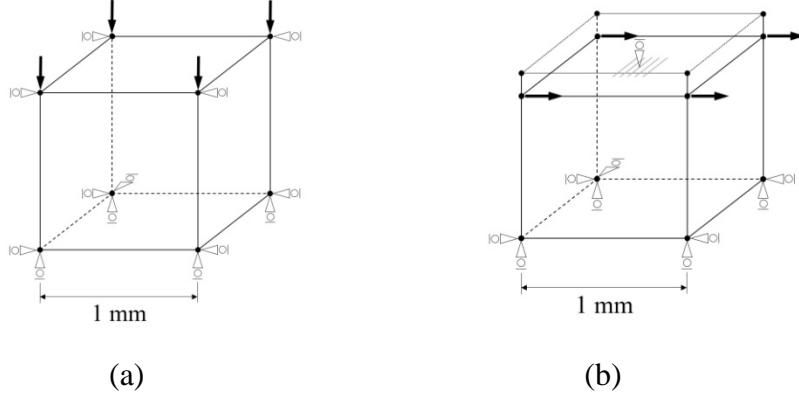


Figure 14. Combined compression-shear test. Dimensions, loading, and boundary conditions for (a) compression step, (b) shear step.

The material constants for the three-invariant model are identical to those in Table 4, for triaxial compression test, except for $q_1 = 0.001$. The shear stress-strain responses for the two frameworks are depicted in Figure 14. The graphs are comparable.

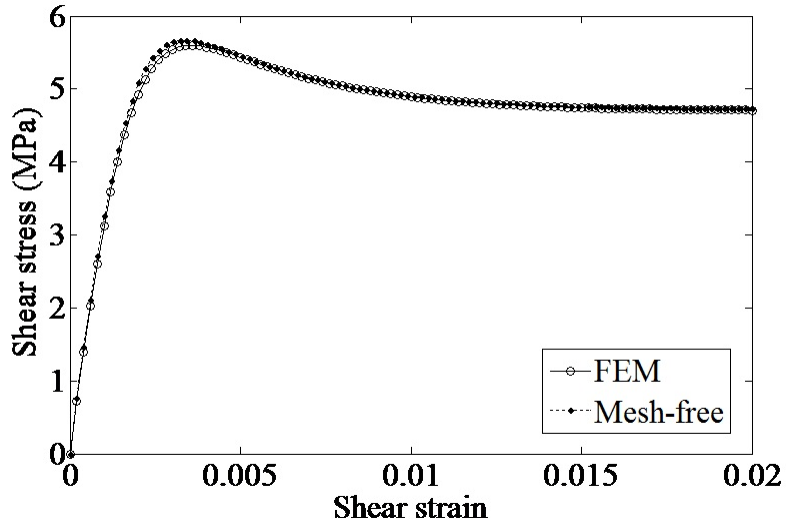


Figure 15. Three-invariant plasticity and combined compression-shear test. Shear stress vs. shear strain for FEM and mesh-free.

5.1.5. Discussion

Throughout Section 5.1.2, given the formulations developed in Section 4.2, most of the salient characteristics of the proposed smooth three-invariant cap model have been tested and verified by a number of numerical examples.

The above examples demonstrate some of the important features of the new model in numerical frameworks as well as verify the two implementations. With regards to the latter, the model has

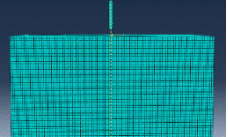
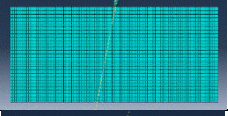
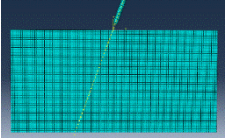
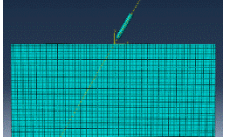
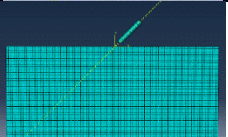
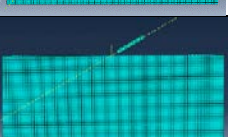
been first verified against the well-known Drucker-Prager model to the extent that the models are comparable. The two models matched up to machine round off error. Comparing the finite element and meshfree implementations of the new model, one can see the two implementations are nearly identical. Small differences are due to the dynamic implementation, albeit with small mass, and explicit global time stepping of the meshfree code, as well as a different number of time steps. In addition, the FEM formulation uses a small strain assumption while the meshfree accounts for large strains.

The examples also verify that the intended features of the models work under uniaxial and multiaxial loading conditions. The hardening and softening behavior of the model is evident in the examples, as is the rate dependence. The new tension cap is also performing as expected. Though not discussed here, the compression cap and the triaxiality functions have also been tested in the finite element framework.

5.2. *Ad hoc* projectile penetration in soil simulations

To demonstrate the capability of the developed two-field meshfree code, ad hoc projectile-soil penetration tests with different impact angles are set up as described in Table 5. The projectile's geometry and soil's dimensions are set up to be the same and an initial velocity of 150 m/s for the projectile is considered for all cases. The dimensions of the soil domain are 16m×12m (the impact surface) with depth of 8m. They are chosen large enough to ensure that reflected waves from the boundaries have minimal influences on the penetration area. To mimic a semi-infinite soil domain, fixed boundary conditions are employed on all surfaces of the soil domain, except the traction-free surface (top impact surface).

Table 5. Problem setup of projectile penetration in soil

Case #	Configuration	Impact Angle (Degrees)
1		90°
2		80°
3		70°
4		60°
5		45°
6		30°

A cylindrical projectile with a radius of 0.2m and a height of 2.5m is selected to mimic the training munitions dropped on the test site. The detailed projectile's dimensions are shown in Figure 15.

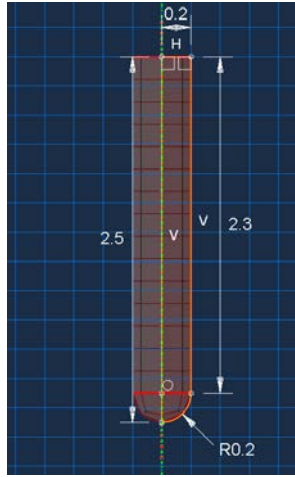


Figure 16. Dimension of projectile

Although the mesh is not required for the meshfree simulation, a standard FEM mesh software is used to create the point discretization for the projectile and the soil domain. The mesh configurations for the projectile and the soil are shown in Figure 16. The nodal distance is fairly uniform for the whole model (projectile and soil), 0.151m on average. This spacing keeps a good balance between accuracy and computational efficiency.

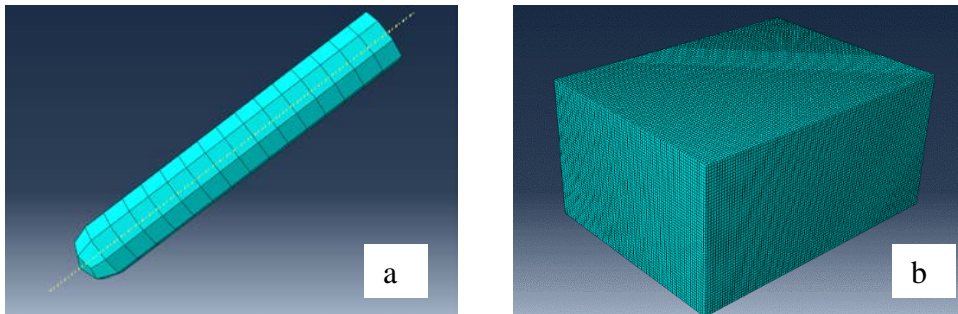


Figure 17. Discretization for the projectile and the soil

In this simulation, the projectile is modeled as linear elastic with properties given in Table 6. The soil is modeled with the non-associative Drucker-Prager model with damage (Section 4.3) under the two-field semi-Lagrangian RK formulation (Section 4.2). The material properties of the soil model are given in Table 7.

Table 6. Material properties of projectile

Linear Elastic Material	
Young's modulus (E)	$2E+11 (\frac{N}{m^2})$
Poisson's ratio (ν)	0.25
Density (ρ)	$8050 (\frac{kg}{m^3})$
Mass proportional damping	0.05

Table 7. Material properties of soil

Drucker-Prager geomaterial properties	
Young's modulus (E)	$2E + 8 (\frac{N}{m^2})$
Poisson's ratio (ν)	0.2
Friction (β)	0.16
Hardening	$1E + 8 (\frac{N}{m^2})$
Cohesion strength (α)	$2E + 4 (\frac{N}{m^2})$
First parameter for damage accumulation function	0.05
Second parameter for damage accumulation function	1.0
Density (ρ)	$2000 (\frac{kg}{m^3})$
Mass proportional damping	0.05

The deformation snapshots of the penetration for each case are given in Figures 18, 20, 22, 24, 26, 28. The color in the plots indicates the level of damage. The time history data for the impact/penetration process in the first 0.2 second are reported in Figures 19, 21, 23, 25, 27, 29. In each case, the results are presented using five different plots:

(a) Trajectory:

This plot shows the projectile-tip's node path during impact and penetration. The maximum depth of penetration can be observed.

(b) Horizontal displacement time history:

This plots shows the horizontal position of projectile's tip with respect to time.

(c) Vertical displacement time history:

This plots shows the vertical position of projectile's tip at each time step. On this plot, the maximum penetration depth and the time it occurs are shown.

(d) Horizontal velocity time history:

This plot shows the horizontal nodal velocity at different times.

(e) Vertical velocity time history:

This plot shows the vertical nodal velocity at different times.

Table 8 shows the maximum penetration depth for all cases:

Table 8. Projectile's maximum penetration depth for different impact angles

Case No. (Impact Angle)	Maximum Penetration Depth (m)
#1 (90°)	3.00
#2 (80°)	2.96
#3 (70°)	2.40
#4 (60°)	2.2
#5 (45°)	1.08
#6 (30°)	0.08

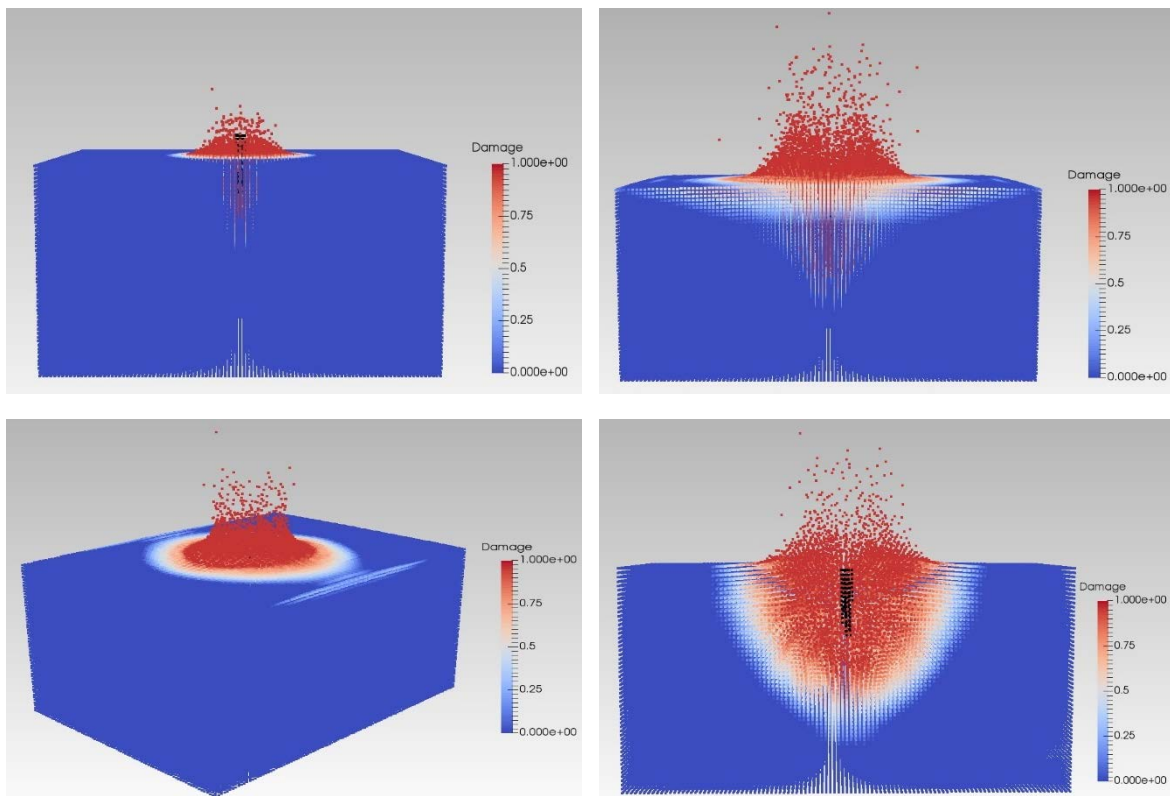


Figure 18. Deformation of penetration in soil (impact angle 90°)

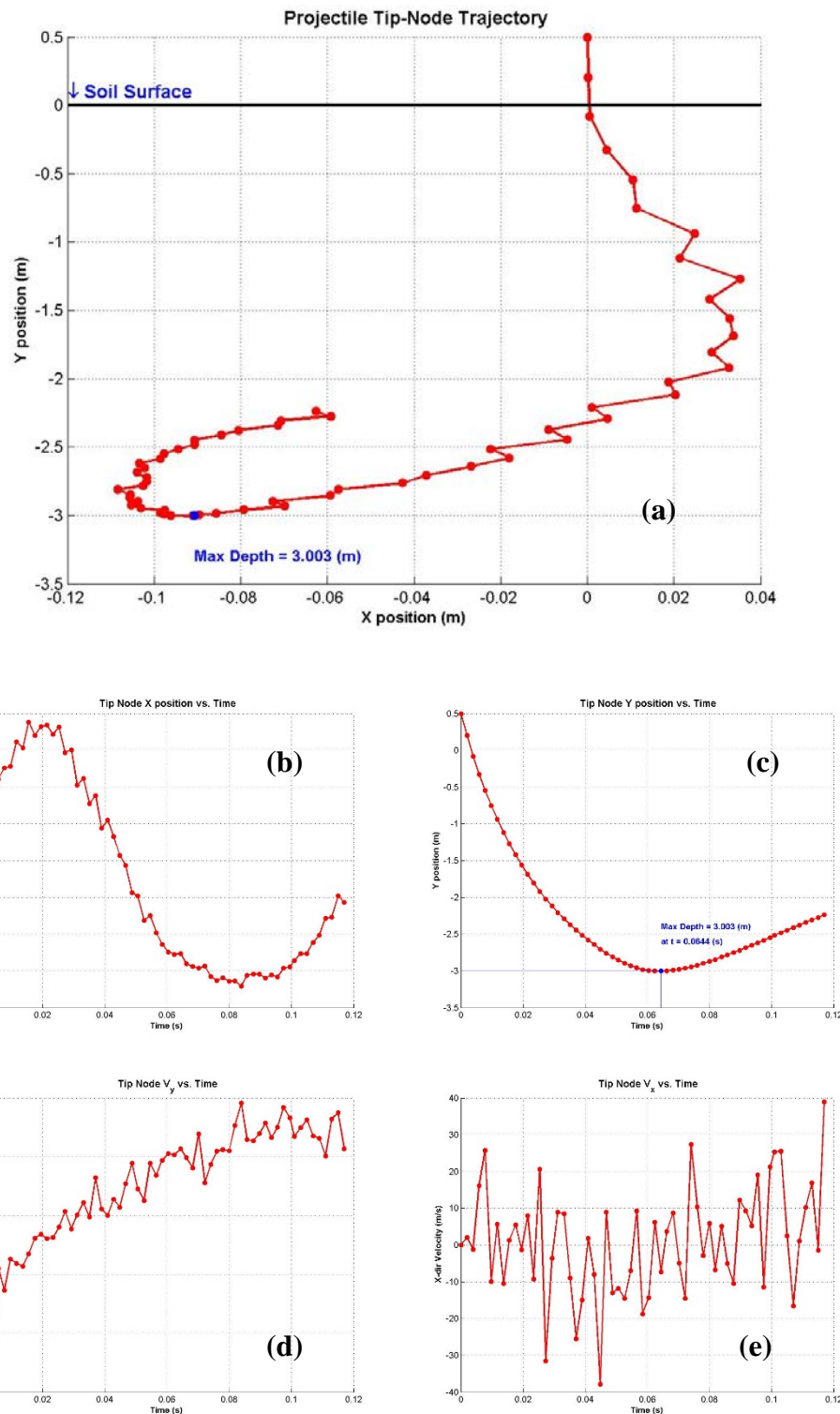


Figure 19. Trajectory and time history of penetration (impact angle 90°). (a) tip trajectory, (b) horizontal displacement history, (c) vertical displacement history, (d) horizontal velocity history, (e) vertical velocity history

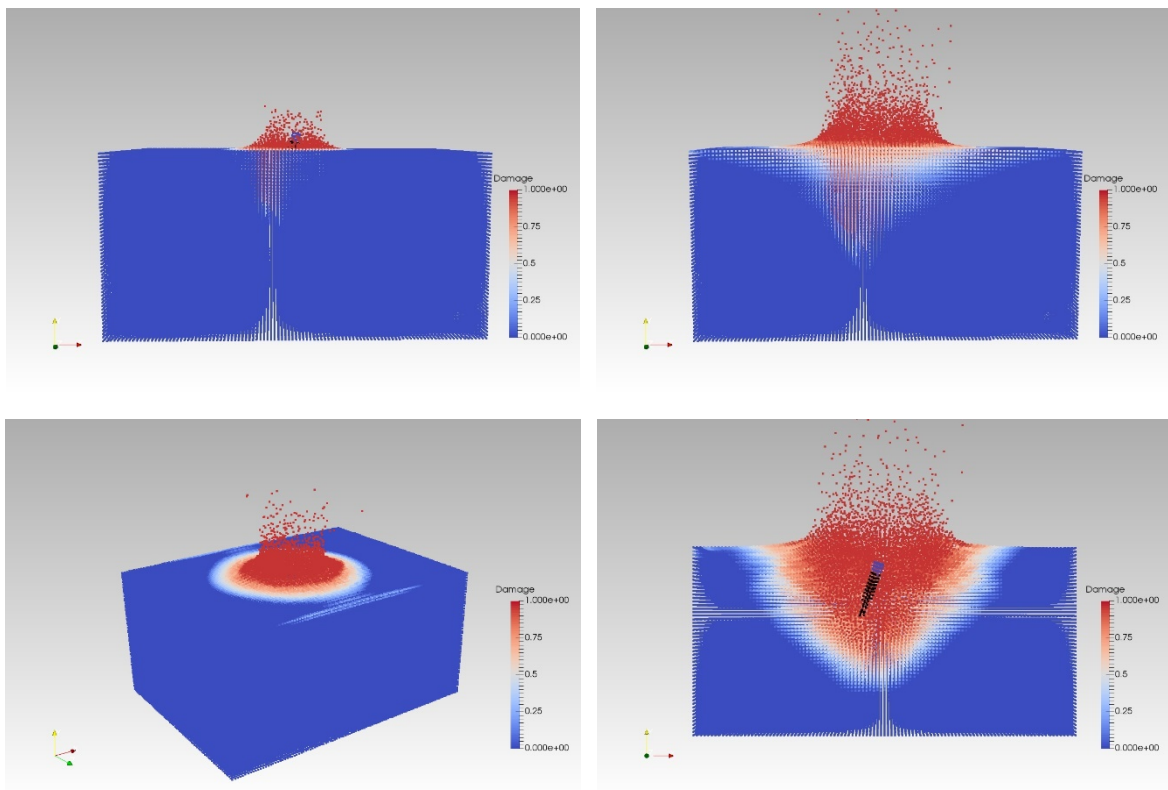


Figure 20. Deformation of penetration in soil (impact angle 80°)

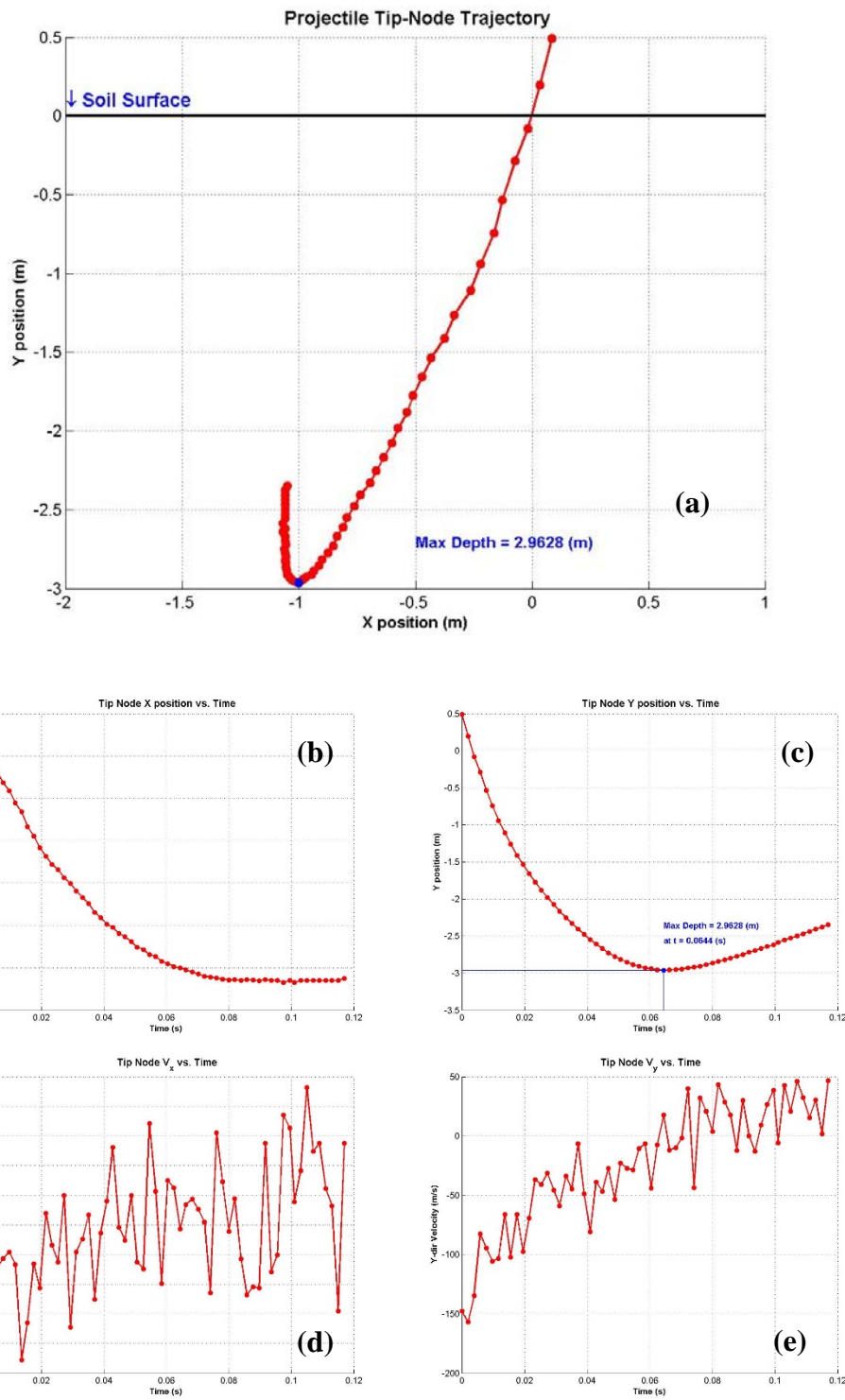


Figure 21. Trajectory and time history of penetration (impact angle 80°). (a) tip trajectory, (b) horizontal displacement history, (c) vertical displacement history, (d) horizontal velocity history, (e) vertical velocity history

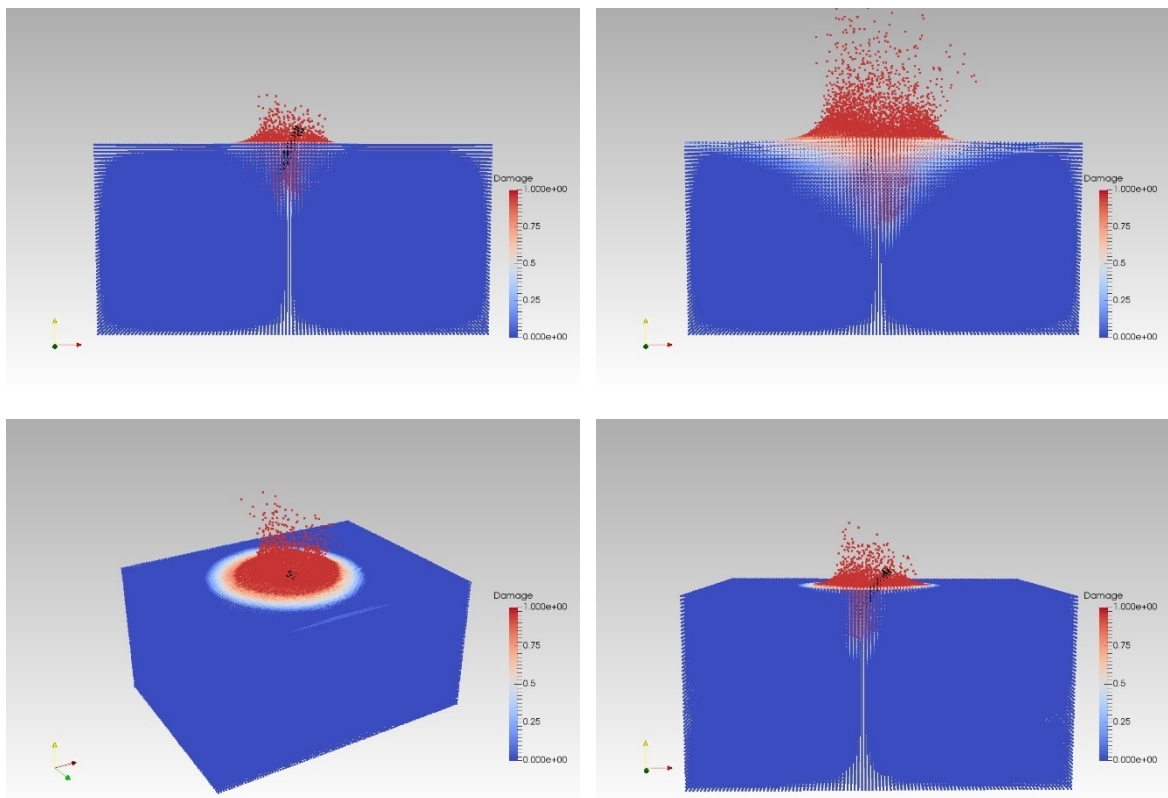


Figure 22. Deformation of penetration in soil (impact angle 70°)

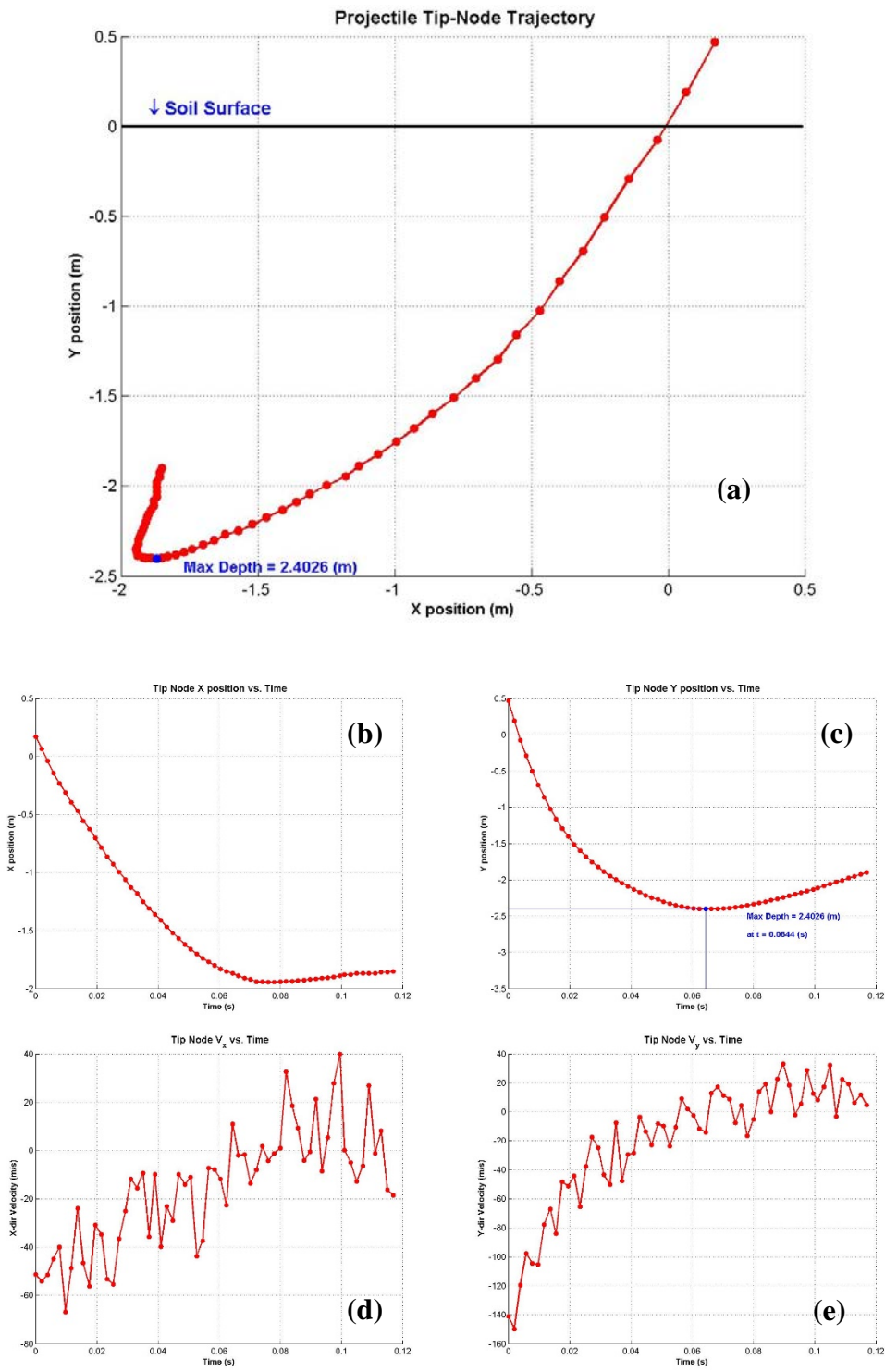


Figure 23. Trajectory and time history of penetration (impact angle 70°). (a) tip trajectory, (b) horizontal displacement history, (c) vertical displacement history, (d) horizontal velocity history, (e) vertical velocity history

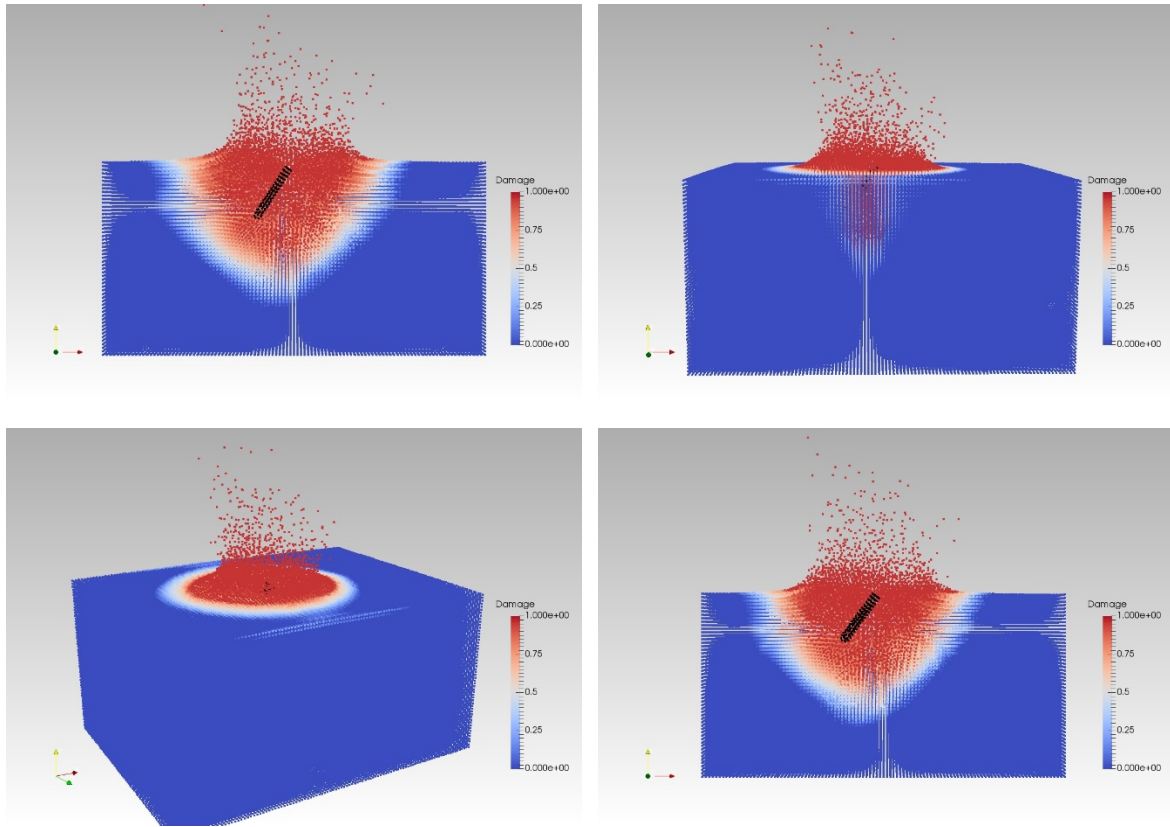


Figure 24. Deformation of penetration in soil (impact angle 60°)

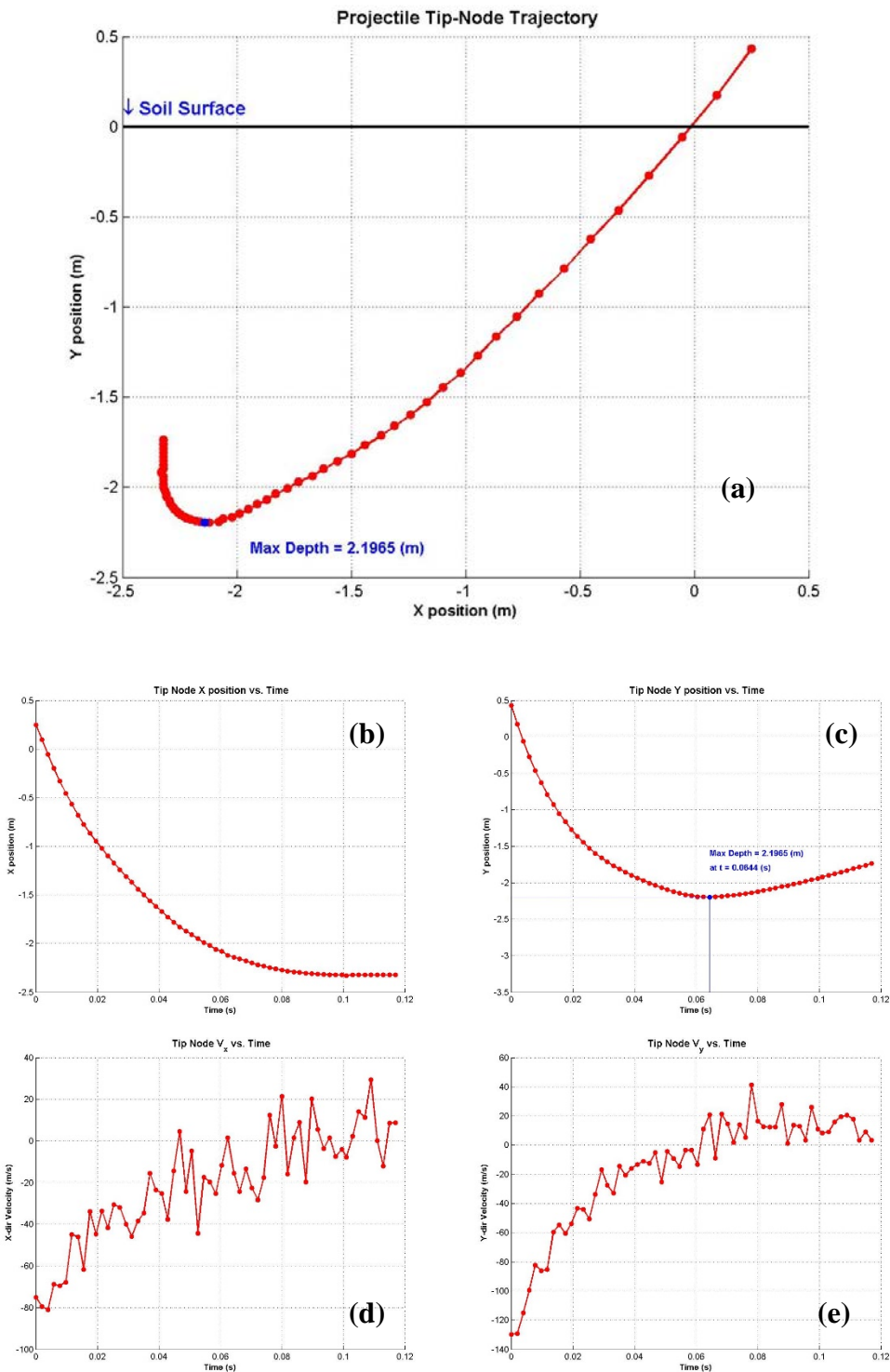


Figure 25. Trajectory and time history of penetration (impact angle 60°). (a) tip trajectory, (b) horizontal displacement history, (c) vertical displacement history, (d) horizontal velocity history, (e) vertical velocity history

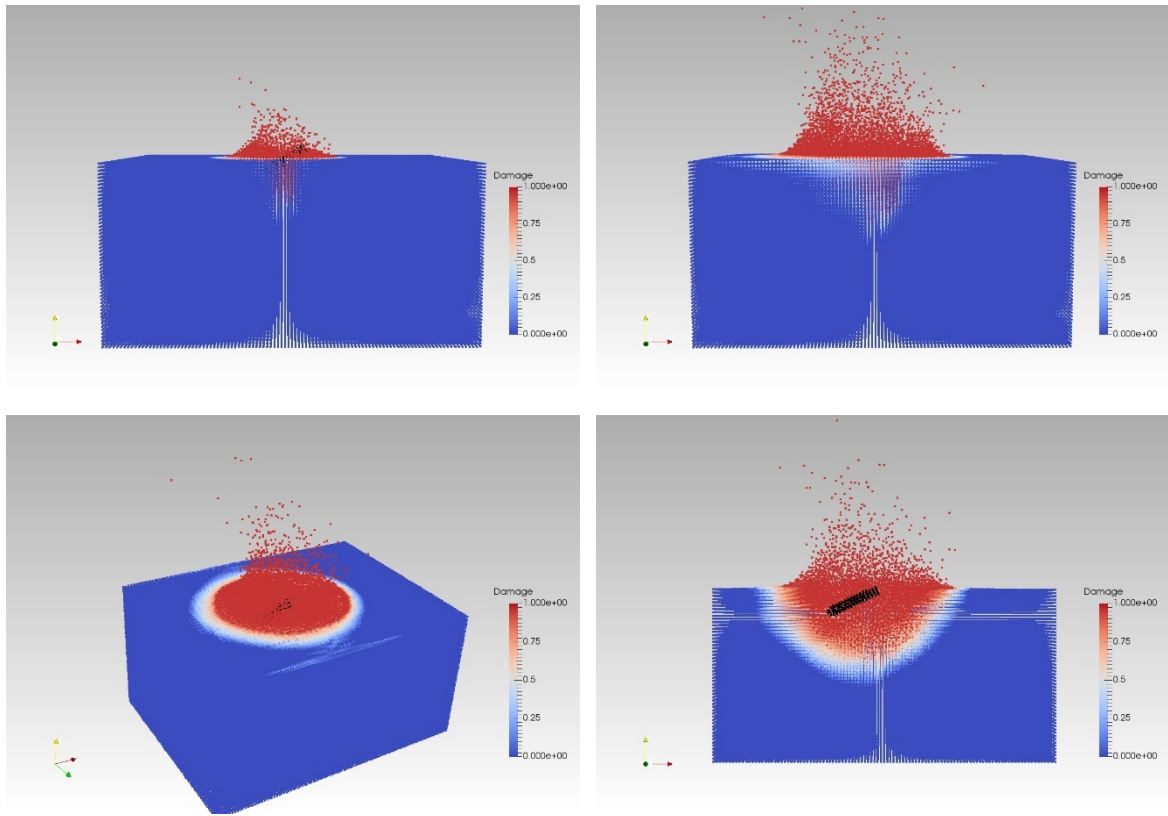


Figure 26. Deformation of penetration in soil (impact angle 45°)

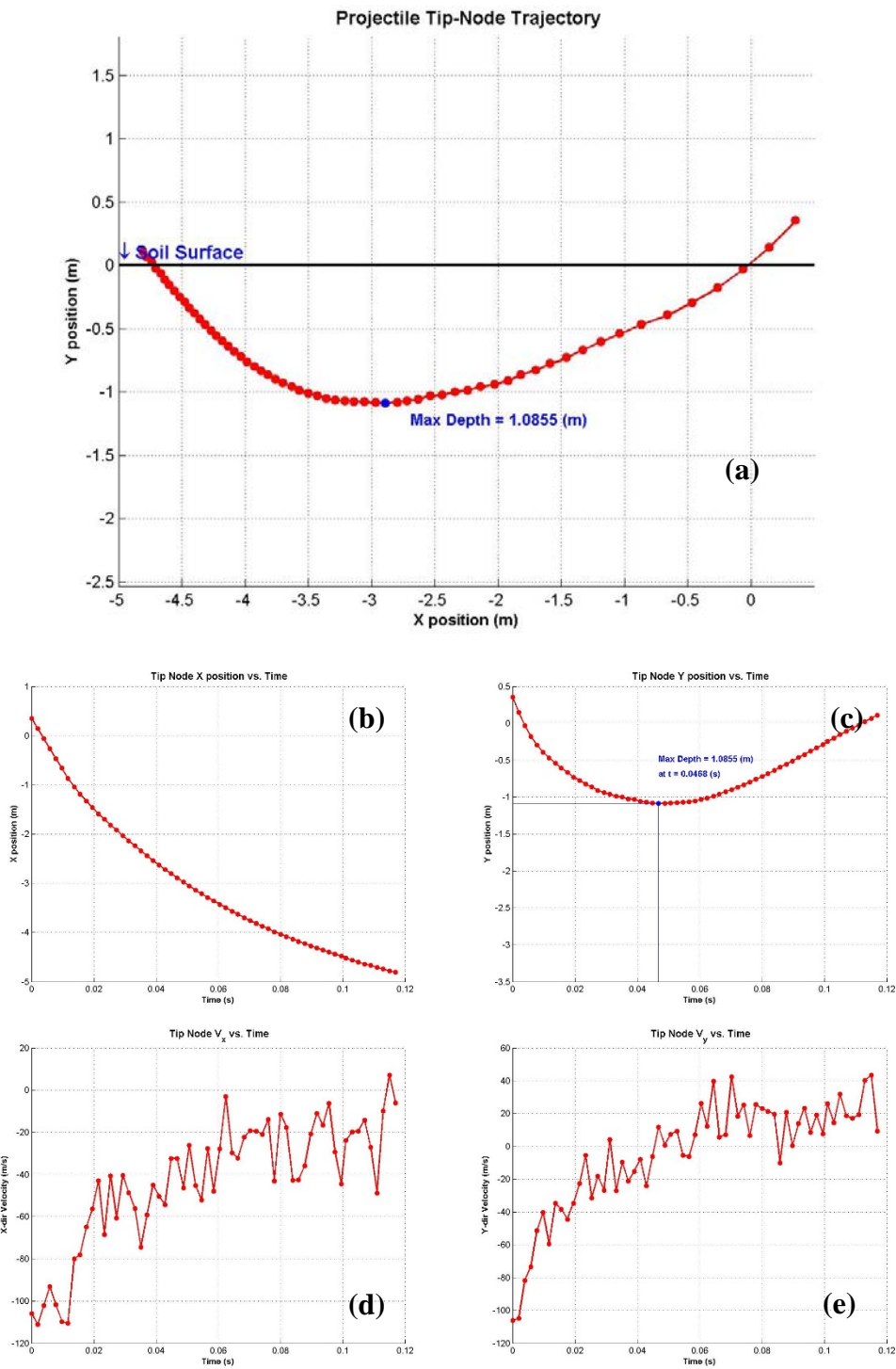


Figure 27. Trajectory and time history of penetration (impact angle 45°). (a) tip trajectory, (b) horizontal displacement history, (c) vertical displacement history, (d) horizontal velocity history, (e) vertical velocity history

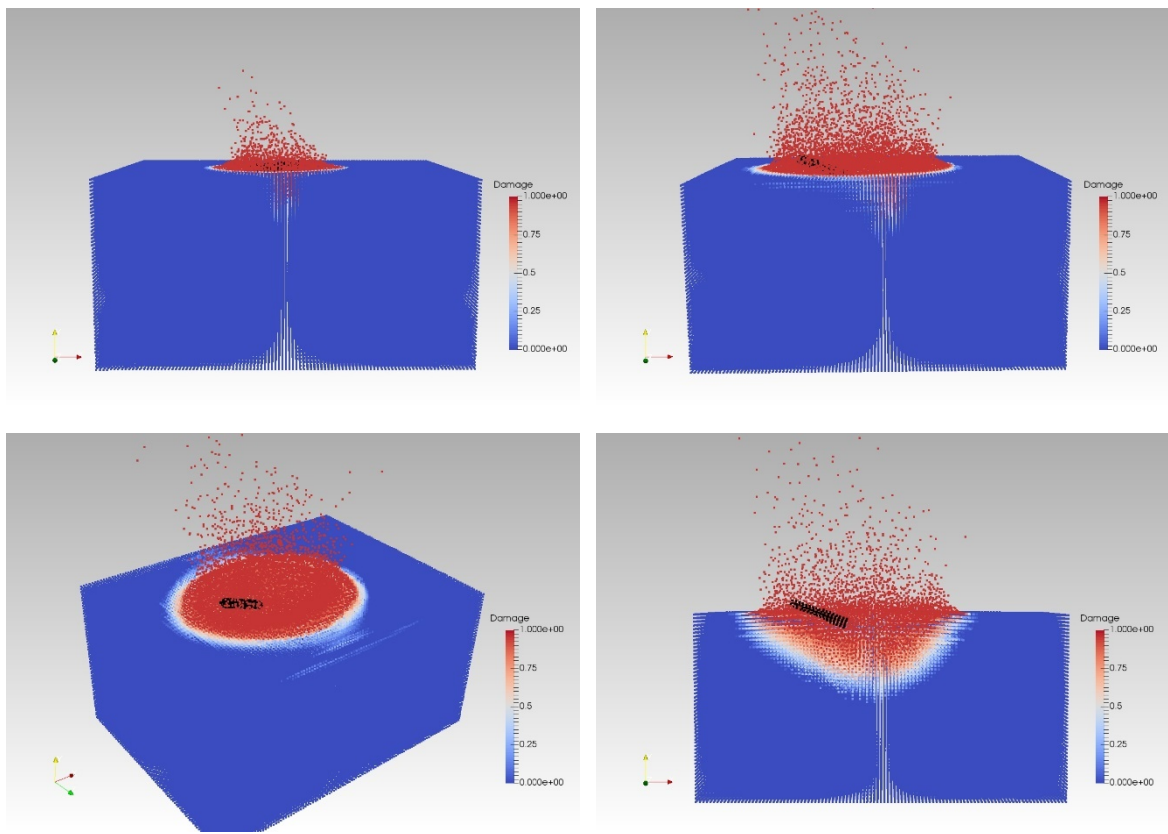


Figure 28. Deformation of penetration in soil (impact angle 30°)

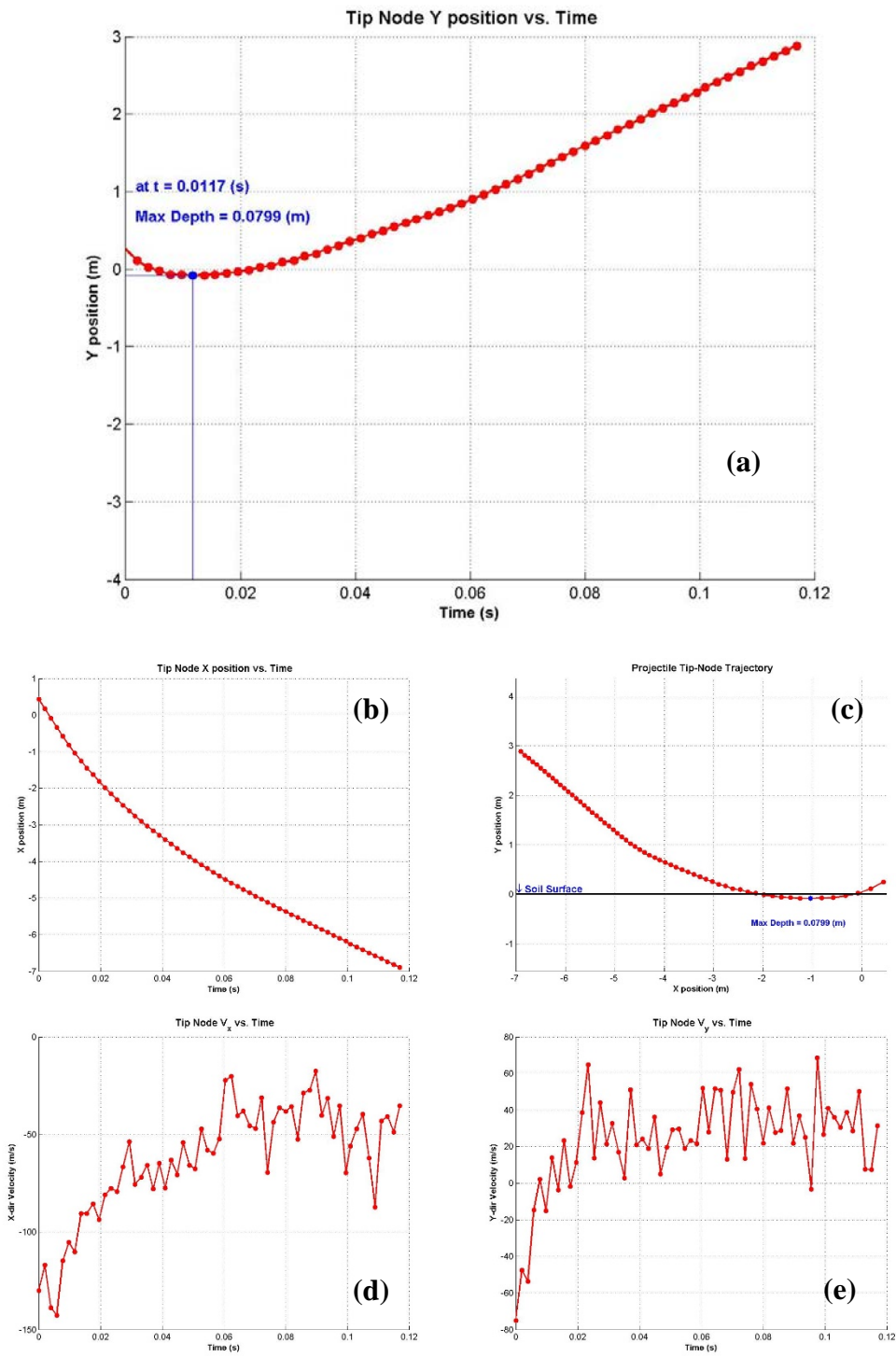


Figure 29. Trajectory and time history of penetration (impact angle 30°). (a) tip trajectory, (b) horizontal displacement history, (c) vertical displacement history, (d) horizontal velocity history, (e) vertical velocity history

5.2.1. Conclusions

Since experimental data for validations of penetration into soil is limited, a complete set of data with different parameters have not found in the public literature. The *ad hoc* simulations in this section is aimed to test the performance of the newly developed and implemented two-field semi-Lagrangian RK code.

Despite no corresponding experimental data available for validation, the simulations demonstrate firstly that stable numerical solutions can be obtained. The stability is a particular concern in this type of simulations. Instability may be caused by nodal domain integration, the approximations for the displacement and pressure fields, explicit temporal integration, and/or combination of abovementioned. The current implementation, with the MSNNI, linear RK for both displacement and pressure field, and explicit temporal integration, provides an effective means to simulate the penetration problems.

Secondly, the basic inelastic impact mechanisms are captured in the simulations: the maximum penetration depth reduces as the impact angle reduces, and reflection angle is smaller than the impact angle. The soil deformation during the penetration also shows material splashing on the free surface, which is commonly seen in similar experiments.

One interesting observation in the numerical test is that the projectile is bouncing back even if the impact angle is close to 90°. This may be attributed to finite boundary conditions, over stiffness, low cohesion, and damping in soil properties. On the other hand, the observation may indeed reflect the physical penetration process happened in the experiments. In such case, the final penetration depth, after splashing material and projectile settle down, is anticipated to be less than the maximum penetration depth. More studies and designed experiments are needed to validate the numerical simulations.

5.3. Simulations of spherical ball drop test

The motivation behind this simulation is constructing a numerical model, by using the calibrated material properties and the Drucker-Prager constitutive model used in the previous section, to reproduce and validate the experimental results reported by (Seguin et al., 2008). For this purpose, a steel-made sphere ball falling under its own weight on an unbounded grain medium is modeled and its maximum penetration has been evaluated. The term unbounded states the fact that the grain container dimensions are chosen to be large enough to decrease the boundary effects on the results to its minimum.

The experimental setup for this test is shown in Figure 30:

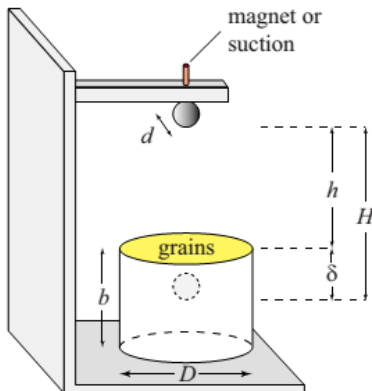


Figure 30. Experimental setup (Seguin, et al 2008)

Variables shown in the Figure 30 described as below:

δ : Maximum penetration depth.

h : Initial distance between the sphere ball's lowest point and grain container's surface.

H : Total drop height after penetration.

d : Sphere ball diameter (19 (mm) for this test)

D : cylindrical container's diameter (190 (mm) for this test)

b : cylindrical container's height (150 (mm) for this test)

In this simulation, three different initial heights (h) of 100, 300, and 500 (mm) are tried. For computational efficiency, for all three cases, the ball is located at the distance of 50 (mm) and corresponding initial velocities are assigned to the ball nodes for each case. For this purpose, the difference of actual total height (h) and the assumed initial numerical height are used by the formula below,

$$v = \sqrt{2g(h - 0.05)}$$

where g is the ground acceleration of 9.806 $\left(\frac{m}{s^2}\right)$ and v is the ball's initial vertical speed.

Table 9 shows the initial velocity for three case. The granular medium consists of glass beads with properties presented in Table 10 and the steel-made ball linear elastic properties are as given in Table 11.

Table 9. Initial position & Velocity for spherical ball

Drop Height (mm)	Height Difference (mm)	Initial Velocity (mm/s)
500	450	2970.85
300	250	2214.34
100	50	990.28

Table 10. Drucker-Prager parameters & properties

Drucker-Prager granular glass beads properties	
Young's modulus (E)	$2.0486E + 8 \left(\frac{N}{m^2}\right)$
Poisson's ratio (ν)	0.3227
Friction (β)	0.1003
Hardening	0.0
Cohesion strength (α)	0.0
First parameter for damage accumulation function	0.05
Second parameter for damage accumulation function	1.0
Density (ρ)	$2500 \left(\frac{kg}{m^3}\right)$
Mass proportional damping	0.05

Table 11. Spherical ball mechanical properties

Linear Elastic Material (steel ball)	
Young's modulus (E)	$2E+11 \left(\frac{N}{m^2}\right)$
Poisson's ratio (ν)	0.25
Density (ρ)	$7800 \left(\frac{kg}{m^3}\right)$
Mass proportional damping	0.05

An average mesh size of 3.5 (mm) of hexahedral element is used for both ball and grain parts. Here the mesh configurations are shown for both parts. Figure 31 shows the mesh configuration for this model.

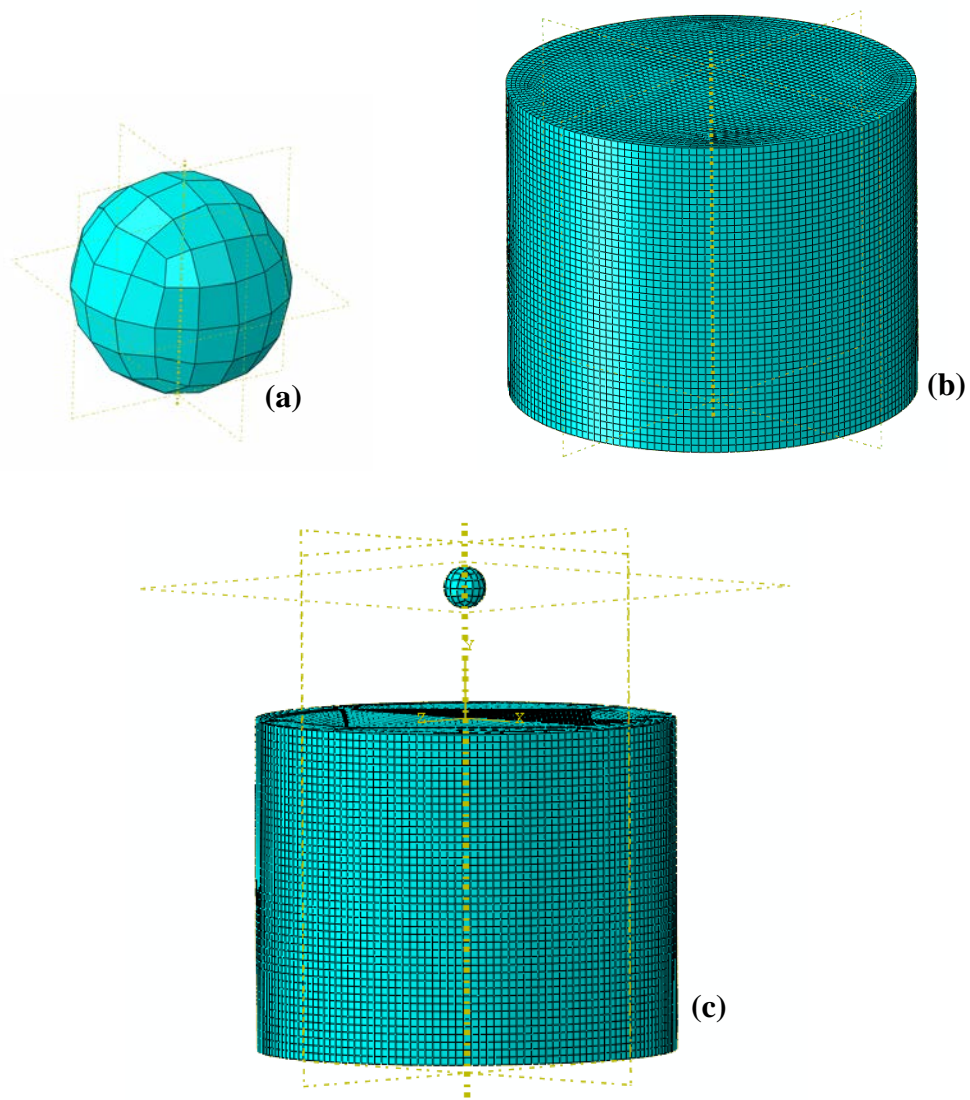


Figure 31. (a) Spherical ball mesh configuration. (b) glass beads medium mesh configuration. (c) Initial ball's position in the numerical model

Figures 32 to 34 show different frames of the test. Figures on the right-hand side show approximately an equal time step of the simulation. As it is clear, the higher the drop height becomes, the more severe the impact is observed.

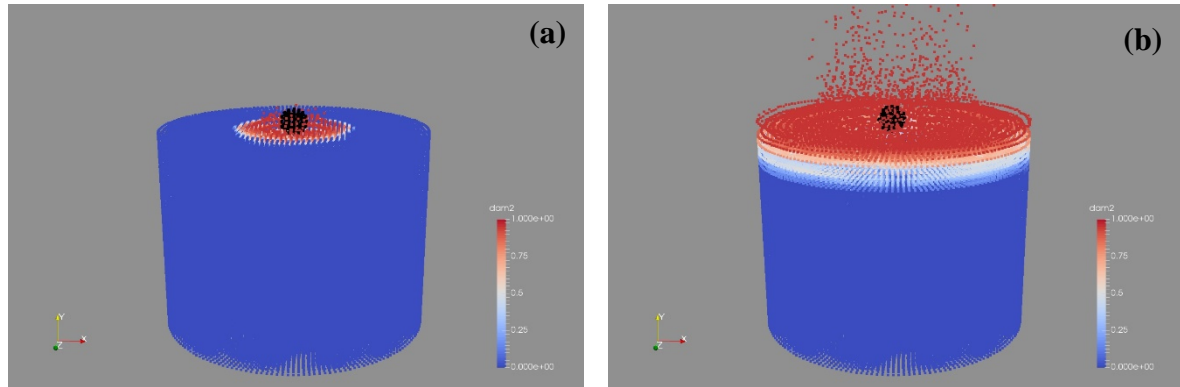


Figure 32. Case1; 500(mm) drop height

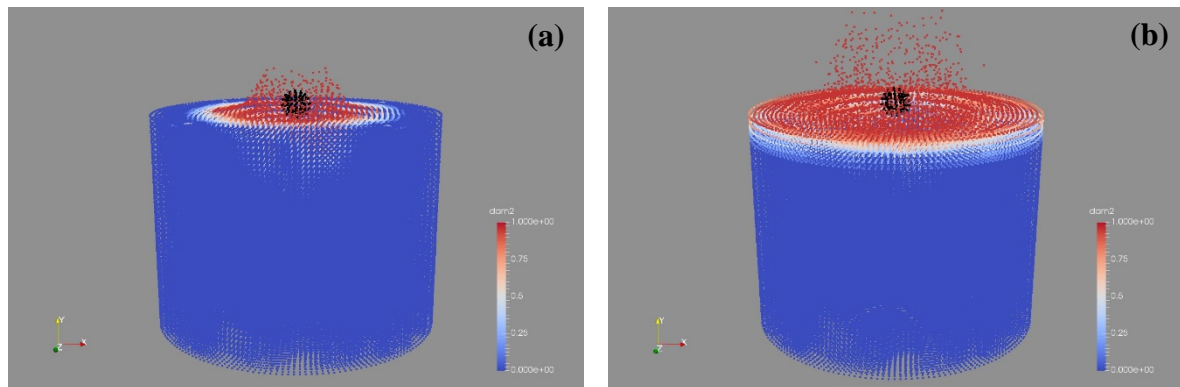


Figure 33. Case2; 300(mm) drop height

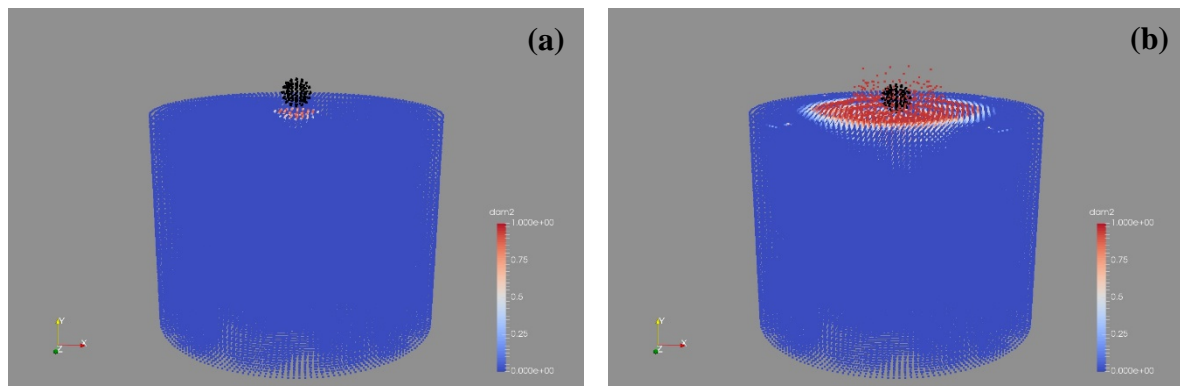


Figure 34. Case3; 100(mm) drop height

Final penetration depth for all three cases are shown in the Table 12:

Table 12. normalized total drop height and penetration depth

δ (mm)	h (mm)	H (mm)	H/d	δ/d	δ/d (Experiment)
1.1207	100	115.8	6.1	0.83	1.4 ± 0.2
5.6147	300	320.4	16.86	1.07	2.4 ± 0.2
7.6883	500	526.3	27.7	1.38	2.85 ± 0.2

As shown in the table above, increasing the ball's release height would result in a higher penetration depth. However, getting better agreement with the experimental data, requires a better means or more experimental testing to calibrate material constants. Figure 35 shows penetration depth along time for the three simulated cases.

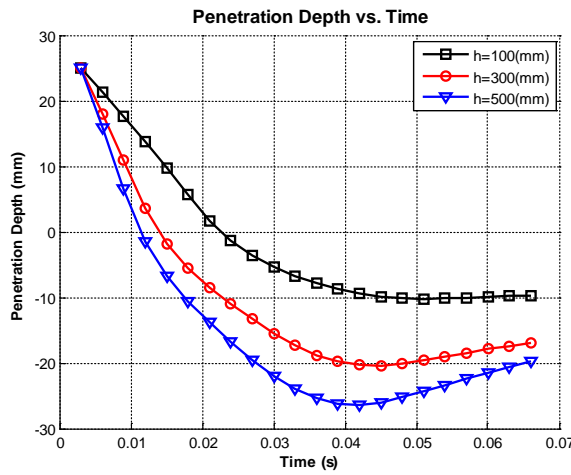


Figure 35. Penetration history for drop test

5.3.1. Discussion

The description of the material parameters of the glass beads in the Seguin, 2008 paper is not complete. We have used estimates of the elastic parameters and friction angle from the literature. Considerable variation in the properties may exist, especially in the initial porosity, which greatly affects fiction angle. The measured elastic modulus also varies significantly for glass beads, and the fitting procedure for the bulk elastic modulus from this is approximated. Finally, the Drucker-Prager model is approximate and does not capture perfectly all of the behaviors of the beads during impact.

As we improve the validation, we will use a few simulations to better fit the bulk elastic and plastic parameters. Those parameters, in turn, will be used perform other simulations not used in the fitting, to validate that the model can capture physical phenomena with accurate input.

6. Conclusions and Implications for Future Research/Implementation

6.1. Conclusions:

The two-field (displacement-pressure) formulation based on Biot theory has been developed and implemented under the semi-Lagrangian RK framework, where displacement and pressure field are independently approximated by the semi-Lagrangian RK shape functions. Numerical schemes originally designed for the single-field formulation have been modified and implemented for the two-field formulation, including the modified stabilized non-conforming nodal integration for the domain integration, stress update, and kernel contact algorithms. The central difference and forward Euler temporal integration schemes have been applied to the displacement and pressure fields, respectively, in the two-field formulation, leading to an explicit time marching scheme.

To present the soil behavior, two constitutive models are updated and implemented in the semi-Lagrangian framework: the Drucker-Prager plasticity with damage model and three invariant viscoplasticity model. In the former model, a single damage parameter is introduced to degrade the deviatoric and tensile parts of the effective stress, providing a simple means to represent material damage and softening.

A three-invariant viscoplasticity model has been developed to effectively integrate tensile, shear, and compressive behavior. The evolution of volumetric plastic strain has been explicitly connected to the void ratio, allowing the model to be integrated with a poromechanical framework. Novel hardening/softening laws to have been added to characterize strengthening and weakening in different loading regimes, and regularized the softening using viscoplasticity. The model also accounts for rate effects, differences in strength in triaxial extension and compression, compression hardening, and other effects. An efficient implementation using the spectral decomposition has been employed to reduce the cost of the complicated model.

The model has been verified against a Drucker-Prager model, and the meshfree and finite element versions of the model have been verified against each other to ensure proper implementation. The behaviors of the model have been demonstrated in a numerical framework using reasonably simple example problems.

The developed two-field meshfree code has been employed to simulate penetration process into soil and predict the final penetration depth under different penetration angles. In the *ad hoc* simulations, the numerical results show that the maximum penetration depth varies from 3m to 1m with penetration angles ranging from 90° to 45°. The deformation of soil, e.g. soil splashing on the free surface, reflects the experiment observations after impact. The developed meshfree code has been used to simulate a spherical ball impact a granular medium (Seguin, 2008). The numerical results, at the current stage, does not agree with the experimental data due to lack of data to calibrate material constant in the simulation and the reasons discussed in the Section 5.3.1. Nevertheless, the numerical results show that the penetration depth increases with the increase of drop height and that the penetration depth increase from the drop height of 100mm to 300mm is higher than that from the drop height of 300mm to 500mm, which agree with experimental observations.

Based on the numerical studies and observations in the preliminary simulations, suggestions to improve the performance of the meshfree code and soil constitutive models and the calibration of material properties are given in the following section.

6.2. Future Research/Implementation:

6.2.1. Infinite boundary in meshfree framework

The physical domain of soil is best described as semi-infinite. The computational domain, however, is limited to a finite domain for efficiency. In the current study, the fixed boundary condition was used for the surfaces that are connected with surrounding soils. The fixed boundary condition, when hit by elastic waves, generates unphysical reflection waves that disturb the desired solutions near the impact areas. To avoid the reflected wave due to boundaries, the computation domain for soil in the project was constructed large enough to avoid the reflected waves interacting with penetration processes. However, when the total simulation time increases, the reflected waves eventually interfere with penetration processes.

A more efficient way to deal with the issues is implementation of the “infinite element” (Zienkiewics et al. 1983) in the meshfree formulation. Through the explicit or implicit enrichment (Chen et al. 2017), the decaying function (Zienkiewics et al., 2013) due to infinite domain can be embedded in the RK approximation for handling the semi-infinite characteristics of the problem. The infinite element can be developed for both the single-field or two-field formulations.

6.2.2. Gradient enhanced stability and quasi linear formulation

The nodal integration, one integration point per node, is computationally efficient in the Galerkin meshfree formulation. This integration scheme, however, has known accuracy and stability issues. Although the Modified Stabilized Nonconforming Nodal Integration has been implemented in the current meshfree code, numerical instability may occur under certain conditions. The numerical stability issues may be attributed to many reasons, such as the under integration in the Galerkin formulation, losing neighbor nodes needed to form the linear basis functions, Eulerian kernels, and up formulation. To address the issue associated with under integration, the advanced stability (Hillman and Chen, 2016) or (Wu et al., 2016) can be implemented in the meshfree code and be extended to two-field formulation. The quasi-linear reproducing kernel (Yreux and Chen, 2017) can be implemented in the two-field formulation to remedy the issues of losing neighbor points, and ultimately to increase the stability of the meshfree framework.

6.2.3. Regularization for damaged/softened material behaviors

Strain softening or damage in the constitutive model causes strain localization and the numerical solutions exhibit pathological discretization sensitivity. The numerical solution does not converge with the refinement of discretization due to loss of ellipticity in the boundary value problem. Many regularization techniques have been proposed to remedy the strain localization and discretization sensitivity issues (de Borst, 2004; Besson, 2011). One of most effective methods is to introduce the strain gradient in the variational equation. However, the strain gradient requires the second derivatives of approximation, making computation very costly. Instead of the direct derivatives, the implicit derivatives can be efficiently obtained under the graduate RK approximation. Therefore, the implicit strain gradient is suggested to be included in the current two-field/multi-field meshfree code.

6.2.4. Constitutive Model Improvements

While the constitutive model implemented reproduces most relevant behaviors of the soil well, further developments can improve both the fidelity of the model and performance of the numerical algorithm. The following are the key improvements of the model proposed to accurately and efficiently reproduce soil behavior.

Currently, the frictional strength of the material is considered constant. In reality, as materials are compacted, interlocking effects and frictional strength increase. We will modify the parameter M to be function of the porosity, increasing as the material is compacted and decreasing as it dilates.

Plastic compaction can also begin in the shear strengthening regime. In order to capture this behavior, we will disconnect the plastic potential variable κ^e from the variable κ . This update will allow the tracking of the volumetric plastic strain separately from the yield surface. A similar evolution law for both κ and κ^e will still be applicable, and hence this modification can be made with rather a rather minor update to the model.

Finally, we will incorporate nonlinear elasticity into the constitutive model. Especially clay soils exhibit a nonlinear elastic response. While the effects of nonlinear elasticity can be approximately captured by modifying the plasticity model, in complicated loading scenarios that involved unloading it is better incorporate nonlinear elasticity. Currently, we are implementing a geometrically nonlinear model that is materially linear between the Kirchhoff stress and Hencky strain, following (de Souza Neto, et al., 2008). Several nonlinear elastic models have been proposed for soils. Borja (2013) reviews several of those models, and we will follow those models, modifying as necessary.

The modified constitutive model will be integrated into a partially saturated soil framework. Currently, we have implemented a fully saturated soil model in conjunction with the plasticity model. The extension the partially saturated case is easier in some respects, in that volumetric locking issues are not likely to be a problem. There are a number of approaches to modeling partially saturated media, see discussions in Coussy, et al., 2004 and Gens, et al. 2006 for details. A solid plasticity model can be incorporated into a partially saturated framework following Borja and White (2010) using a generalized effective stress. This will be the initial approach for the new implementation.

6.2.5. Numerical Implementation Improvements for soil models

Furthermore, we will investigate methods to improve the efficiency and robustness of the numerical algorithm. Because the return mapping perpendicular to the hydrostatic axis is nearly the same in the trial and final states, it may be possible to use the trial value of the stress gradient of this part of the plastic potential, leading to a scalar equation to be solved rather than a matrix equation. Furthermore, because this part of the return is bounded radially, it may not affect stability. We will formally investigate the accuracy and stability implications of this approach, as well as the gains in efficiency.

Another alternative is to implement a semi-implicit (e.g. Belytschko et al., 2000) or explicit implementation, since the global time stepping scheme is already explicit. This will not affect the order of accuracy but may somewhat reduce the time step needed for stability.

6.2.6. Multiscale material modeling for calibration of material properties

One of the main causes of discrepancy between the numerical results and experimental data is the material constant calibration. While some well-controlled experiments report data for penetration process, the necessary tests for calibration of material constant for soil constitutive models may not be provided or conducted. Moreover, in the meso- or micro- scale, the continuum theory may not be applicable for granular materials. A multiscale framework is therefore recommended. In the meso- or micro-scale, the discrete element method (DEM) can be applied to obtain the mechanical behavior of the granular materials within a representative volume element (RVE). Then the stress-strain relationship of the granular material occupying the RVE can be homogenized and passed to the continuum models in the macroscale (Andrade an Tu, 2009; Andrade, et al., 2011; Ren et al., 2011).

6.2.7. Parametric studies and suggestion of penetration equations

Once the accuracy and robustness of the meshfree is verified and validated, parametric studies can be conducted to understand and/or predict how different penetration parameters affect the final penetration depth for various soil types. Ultimately, penetration equations can be suggested based on simulations.

7. Literature Cited

- L. R. Alejano and A. Bobet, "Drucker–Prager Criterion," *Rock Mech Rock Eng*, 2012. 45, pp.995–999.
- Andrade, J.E., and Tu, X., "Multiscale framework for behavior prediction in granular media," *Mechanics of Materials*, 2009. 41(6): 652-669.
- Andrade, J.E., Avila, C.F., Hal, S.A., Lenoir, N., and Viggiani, G., "Multiscale modeling and characterization of granular matter: From grain kinematics to continuum mechanics," *Journal of the Mechanics and Physics of Solids*, 2011. 59(2):237-250.
- I. Babuška, R. Narasimhan, The Babuška-Brezzi condition and the patch test: an example, *Computer Methods in Applied Mechanics and Engineering*, 1997. 140: 183-199.
- Belytschko, T., Lu, Y. Y., and Gu, L., Element-free Galerkin methods. *Int. J. Numer. Meth. Eng.*, 1994. 37, 229-256.
- Belytschko, T., Liu, W.K., and Moran, B., Nonlinear Finite Elements for Continua and Structures, 1st edition, 2000. Wiley.
- Besson J, "Continuum models of ductile fracture: A review," *International Journal of Damage Mechanics*, 2010. 19: 3–52.
- Biot, M. A. "General solutions of the equations of elasticity and consolidation for a porous material." *J. appl. Mech* 23.1 (1956): 91-96.
- Bonet J, Lok T-SL. Variational and momentum preserving aspects of smoothed particle hydrodynamics (SPH) formulations. *Computer Methods in Applied Mechanics and Engineering* 1999; 180(1-2):97–116.
- Borg JP, Morrissey M, Perich C, Vogler T, Chhabildas L. In situ velocity and stress characterization of a projectile penetrating a sand target: experimental measurements and continuum simulations. *Int J Impact Eng* 2013;51:23-35.
- Ronaldo I Borja, Kossi M Sama, and Pablo F Sanz. On the numerical integration of three-invariant elastoplastic constitutive models. *Computer Methods in Applied Mechanics and Engineering*, 192(9):1227–1258, 2003.
- Borja, R.I. and J.A. White, Continuum deformation and stability analyses of a steep hillside slope under rainfall infiltration. *Acta Geotechnica*, 2010. 5(1): p. 1-14.
- Borvik, T., Dey, S., Olovsson, L., Penetration of granular materials by small-arms bullets. *International Journal of Impact Engineering*, 2015. 75: p. 123-139.
- Ignacio Carol, Pere C Prat, and Carlos M López. Normal/shear cracking model: application to discrete crack analysis. *Journal of engineering mechanics*, 123(8):765–773, 1997.
- Carter JP, Booker JR, Yeung SK. Cavity expansion in cohesive frictional soils. *Geotechnique* 1986;36(3):349-58.

Chen, J.S., Pan, C., Wu, C.T., and Liu, W.K., Reproducing kernel particle methods for large deformation analysis of nonlinear structures. *Computer Methods in Applied Mechanics and Engineering*, 1996. 139, 195-227.

Chen, J.S., Wu, C.T., Yoon, S., and You, Y., 2001. A Stabilized Conforming Nodal Integration for Galerkin Meshfree Methods. *International Journal for Numerical Methods in Engineering*, 50, 435-466.

Chen, J.S., Wu, C.T., Yoon, S., and You, Y., 2002. Nonlinear Version of Stabilized Conforming Nodal Integration for Galerkin Meshfree Methods, *International Journal for Numerical Methods in Engineering*, 53, 2587-2615.

Chen, J.S., W. Hu, M. Puso, Y. Wu, and X. Zhang, *Strain Smoothing for Stabilization and Regularization of Galerkin Meshfree Method*. Lecture Notes in Computational Science and Engineering, 2006. 57: p. 57-76.

Chen, J.S., M. Hillman, and M. Ruter, *An arbitrary order variationally consistent integration for Galerkin meshfree methods*. International Journal for Numerical Methods in Engineering, 2013. 95(5): p. 387-418.

Chen, J.S., Hillman, M., and Chi, S.W., "Meshfree Methods: Progress Made after 20 Years," *Journal of Engineering Mechanics*, 2017. (in press)

Chi, S.W., Lee, C.H., Chen, J.S., and Guan, P.C., A level set enhanced natural kernel contact algorithm for impact and penetration modeling, *International Journal for Numerical Methods in Engineering*, 2015.

Chi, S.W., Siriaksorn, T., and Lin, S.P., "Von Neumann Stability Analysis of the u-p Reproducing Kernel Formulation for Saturated Porous Media," *Computation Mechanics*, 2017. 59(2), pp. 335-357.

Christensen, B.K. Twenty-five Years of Penetration Records at Sandia National Laboratories: PENTDB: a Relational Database. Sandia National Laboratories, 1990.

Coussy, O., *Poromechanics*, 2004. Wiley.

de Borst R, Damage, Material Instabilities, and Failure. *Encyclopedia of Computational Mechanics*, Vol. 2: Solids and Structures. 2004. Wiley: Chichester, pp. 335–373.

Drucker DC, Prager W, "Soil mechanics and plastic analysis or limit design," *Q Appl Math* 1952. 10:157–165

Durban D, Masri R. Dynamic spherical cavity expansion in a pressure sensitive solid. *Int J Solids Struct* 2004;41(20):716.

Euler L. *Neue Grundsätze der Artillerie*. Berlin; reprinted as Euler's Opera Omnia. 1st ed. Berlin: Druck und Verlag Von B. G. Teubner; 1922. p. 484.

Forrestal MJ, Luk VK. Penetration into soil targets. *Int J Impact Eng* 1992;12(3):427-44.

Arlo F Fossum and Rebecca M Brannon. The sandia geomodel: theory and users guide. 2004a.

Fossum A.F., Brannon, R.M., Unified compaction/dilation, strain-rate sensitive, constitutive model for rock mechanics structural analysis applications, 2004b. Gulf Rocks. ARMA/NARMS 04-546.

Foster, C.D., R.A. Regueiro, A.F. Fossum, and R.I. Borja, Implicit numerical integration of a three-invariant, isotropic/kinematic hardening cap plasticity model for geomaterials. Computer Methods in Applied Mechanics and Engineering, 2005. 194(50-52): p. 5109-5138.

Foster, C.D., R.I. Borja, and R.A. Regueiro, Embedded strong discontinuity finite elements for fractured geomaterials with variable friction. International Journal for Numerical Methods in Engineering, 2007. 72(5): p. 549-581.

Gens, Antonio, Marcelo Sánchez, and Daichao Sheng. "On constitutive modelling of unsaturated soils." *Acta Geotechnica* 1.3 (2006): 137-147.

Guan, P.C., Chi, S.W., Chen, J.S., Slawson, T.R., and Roth, M.J. Semi-Lagrangian reproducing kernel particle method for fragment-impact problems, *International Journal of Impact Engineering*, 2011. 38: p. 1033-1047.

P.C. Guan, J.S. Chen, Y. Wu, H. Teng, J. Gaidos, K. Hofstetter, M. Alsaleh, Semi-Lagrangian reproducing kernel formulation and application to modeling earth moving operations, *Mechanics of Materials*, Volume 41, Issue 6, June 2009, Pages 670-683.

G. Gudehus. Elastoplastische stoffgleichungen fr trockenen sand. *Ingenieur-Archiv*, 42(3):151–169, 1973.

Hillman, M., Chen, J.S., and Chi, S.W., Stabilized and Variationally Consistent Nodal Integration for Meshfree Modeling of Impact Problems, *Computational Particle Mechanics*, 2014. 1(2): p. 245-256.

Hillman, M. and Chen, J.S., “An accelerated, convergent, and stable nodal integration in Galerkin meshfree methods for linear and nonlinear mechanics,” *International Journal for Numerical Methods in Engineering*, 2016. 107(7), pp. 603-630.

E. A. de Souza Neto, D. Perić, D. R. J. Owen, *Computational Methods for Plasticity: Theory and Applications*, Wiley, Chichester, 2008.

Dolbow, J., Belytschko, T., Numerical integration of the Galerkin weak form in meshfree methods. *Computational Mechanics*, 1999. 23, 219-230.

Duvaut, G., and Lions, J. L., 1972, “Les Inequations en Mechanique et en Physique,” *Travaux et Recherches*, Vol. 21, Dunod, Paris.

Li, S., Qian, D., Liu, W.K., and Belytschko, T., “A meshfree contact-detection algorithm,” *Computer Methods in Applied Mechanics and Engineering*, 2001. 190(24-25), pp. 3271–3292.

Liu, W.K., Jun, S., and Zhang, Y.F., Reproducing Kernel Particle Method. *Int. J. Numer. Methods Fluids*, 1995. 20, 1081-1106.

M.H. Motamedi and C.D. Foster "An improved implicit numerical integration of a non-associated, three- invariant cap plasticity model with mixed isotropic-kinematic hardening for geomaterials." International Journal of Numerical and Analytical Methods in Geomechanics. 2017. In press.

Omidvar, M., Iskander, M., and Bless, S., Response of Granular Media to Rapid Penetration. International Journal of Impact Engineering, 2014. 66: p. 60-82.

Onate E, Rojek J. Combination of discrete element and finite element methods for dynamic analysis of geomechanics problems. Comput Methods Appl Mech Eng 2004; 193:3087-3128.

Regueiro, R.A. and C.D. Foster, Bifurcation analysis for a rate-sensitive, non-associative, three-invariant, isotropic/kinematic hardening cap plasticity model for geomaterials: Part I. Small strain. International Journal for Numerical and Analytical Methods in Geomechanics, 2011. 35(2): p. 201-225.

Ren, X., Chen, J. S., Li, J., Slawson, T. R., Roth, M. J., "Micro-cracks Informed Damage Models for Brittle Solids," International Journal of Solids and Structures, Vol. 48, 1560–1571, 2011.

Roscoe K. H. and Burland J. B., "On the generalised stress-strain behaviour of 'wet clay' ", Engineering Plasticity, Heyman and Leckie (ed), 1968. pp.535-609.

Salgado R, Mitchell JK, Jamiolkowski M. Cavity expansion and penetration resistance in sand. J Geotech Geoenviron Eng 1997;123(4):344-354.

Scott, R., 1985, "Plasticity and Constitutive Relations in Soil Mechanics," J. Geotech. Eng., 111(5), pp. 559–605.

Seguin A, Bertho Y, and Gondret P. (2008) Influence of confinement on granular penetration by impact. Physical Review E 78, 010301 (R).

Simo, J.C., and Hughes, T.J.R., Computational Inelasticity, Springer, 1998.

Silling S (2000) Reformulation of elasticity theory for discontinuities and long-range. J Mech Phys Solids 48(1):175

Silling S, Lehoucq R (2008) Convergence of peridynamics to classical elasticity theory. J Elast 93(1):13.

Siriaksorn, T., Chi, S.W., and Foster, C.D., "u-p Semi-Lagrangian Reproducing Kernel Formulation for Landslide Modeling," International Journal for Numerical and Analytical Methods in Geomechanics, 2017. (under revision)

de Souza Neto, E. A., Peric, D., and Owen, D. R. J., 2008, Computational Methods for Plasticity, Wiley, New York.

Claudio Tamagnini, Riccardo Castellanza, and Roberto Nova. A generalized backward euler algorithm for the numerical integration of an isotropic hardening elastoplastic model for

mechanical and chemical degradation of bonded geomaterials. *International Journal for Numerical and Analytical Methods in Geomechanics*, 26(10):963–1004, 2002.

Tiwari, M., Mohan, T.R.K., and Sen. S., Drag-force regimes in granular impact. *Physical Review E*, 2014. 90(6): 062202.

Wu, C.T., Chi, S.W., Koishi, M., and Wu, Y., “Strain gradient stabilization with dual stress points for the meshfree nodal integration method in inelastic analyses,” *International Journal for Numerical Methods in Engineering*, 2016. 107(1), pp. 3-30.

Yreux, E. and Chen, J.S., “A quasi-linear reproducing kernel particle method,” *International Journal for Numerical Methods in Engineering*, 2017. 109(7), pp. 1045-1064.

Yu HS, Houlsby GT. Finite cavity expansion in dilatant soils: loading analysis. *Geotechnique* 1991;41(2):173-183.

Zienkiewicz, O.C., Emson, T.C., and Bettesso, P., “A novel boundary infinite element,” *International Journal for Numerical Method in Engineering*, 1983. 19, pp. 393-404.

Zienkiewicz, O. C., Taylor, R.L., and Zhu, J.Z., *The Finite Element Method: Its Basis and Fundamentals*, 7th Edition, 2013. Elsevier.

8. Appendices

A. Supporting Data:

None.

B. List of Scientific/Technical Publications

Peer-reviewed journals:

- Chi, S.W., Siriaksorn, T., and Lin, S.P., "Von Neumann Stability Analysis of the u-p Reproducing Kernel Formulation for Saturated Porous Media," Computation Mechanics, 2017. 59(2), pp. 335-357.
- Chen, J.S., Hillman, M., and Chi, S.W., "Meshfree Methods: Progress Made after 20 Years," Journal of Engineering Mechanics, 2017. (in press)
- Siriaksorn, T., Chi, S.W., and Foster, C.D., "u-p Semi-Lagrangian Reproducing Kernel Formulation for Landslide Modeling," International Journal for Numerical and Analytical Methods in Geomechanics, 2017. (under revision)

Conference abstracts:

- Chi, S.W., Siriaksorn, T., and Mahdavi, A., "Mixed-field Meshfree Method for Modeling Munitions Penetration in Soils," EMI 2016/PMC 2016, May 22-25, 2016, Nashville.
- Chi, S.W. and Siriaksorn, T., "Stability Analysis of u-p Reproducing Kernel Formulation for Saturated Porous Media," WCCM XII & APCOM VI, July 24-29, 2016, Seoul, Korea.
- Chi, S.W., Siriaksorn, T., and Mahdavi, A., "Strain Gradient Stabilization with Dual Stress Points in the Reproducing Kernel Formulation for Modeling Penetration in Soils," USACM Conference on Isogeometric Analysis and Meshfree Methods, October 10-12, 2016, La Jolla, CA.
- Foster, C.D., Chi, S.W., Parvaneh S.M., and Madhavi A. "Modeling extreme soil deformation for soil penetration problems". International Conference on Plasticity, Damage, and Fracture, January 3-9, 2017. Puerto Vallarta, Mexico.

C. Other Supporting Materials

None.